Applied Materials Today 13 (2018) 242–270

Contents lists available at ScienceDirect

Applied Materials Today

journal homepage: www.elsevier.com/locate/apmt

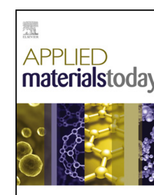

Review

2D layered transition metal dichalcogenides (MoS_2): Synthesis, applications and theoretical aspects

Arun Kumar Singh[a,1], P. Kumar[b,1], D.J. Late[b], Ashok Kumar[c], S. Patel[d], Jai Singh[d,*]

[a] Department of Physics, Motilal Nehru National Institute of Technology, Allahabad 211004, India
[b] Physical & Materials Chemistry Division, National Chemical Laboratory, Pashan Road, Pune 411008, India
[c] Department of Physical Sciences, School of Basic and Applied Sciences, Central University of Punjab, Bathinda 151001, India
[d] Department of Physics, Dr. H.S.G. University, Sagar, 470003, India

A R T I C L E I N F O

Article history:
Received 10 July 2018
Received in revised form 7 September 2018
Accepted 10 September 2018

Keywords:
Two-dimensional materials
Transition metal dichalcogenides
MoS_2
Transistors
Sensors
Solar cell
Field emission
Topological properties

A B S T R A C T

Recently, graphene and other two-dimensional (2D) transition metal dichalcogenides (TMDCs) have been widely explored due to their unique optical, mechanical, electrical and sensing properties for versatile electronic and optoelectronic applications. The atomically thin layers of TMDC materials have shown potential to replace state-of-the-art silicon-based technology. Graphene has already revealed an excess of new physics and multifaceted applications in several areas. Similarly, mono-layers of TMDCs such as molybdenum disulfide (MoS_2) have also shown excellent electrical and optical properties possessing a direct band-gap of ~1.8 eV combined with high mechanical flexibility. In contrast to semi-metallic graphene, the semiconducting behavior of MoS_2 allows it to overcome the deficiencies of zero-band-gap graphene. This review summarizes the synthesis of 2D MoS_2 by several techniques, i.e., mechanical and chemical exfoliation, RF-sputtering, atomic layer deposition (ALD) and chemical vapor deposition (CVD), etc. Furthermore, extensive studies based on potential applications of MoS_2 such as the sensor, solar cells, field emission and as an efficient catalyst for hydrogen generation has been included. Theoretical aspects combined with the experimental observations to provide more insights on the dielectric, optical and topological behavior of MoS_2 was highlighted.

© 2018 Published by Elsevier Ltd.

Contents

1. Introduction 243
 1.1. Benefits of MoS_2 over Silicon 243
2. Properties of transition metal dichalcogenides 244
 2.1. Crystal structures 244
 2.2. Electronic band structures 244
 2.3. Electrical and optical properties 245
 2.4. Vibrational properties 247
 2.5. Mechanical properties 247
3. Theoretical aspects 249
 3.1. First principles perspective of MoS_2 249
 3.2. Background 250
 3.3. Electronic structure of MoS_2 as a function of layers thickness 251
 3.4. Dielectric response of MoS_2: electron energy loss spectroscopy 252
 3.5. A topological aspect of MoS_2 253
 3.6. Topological Z_2 invariant 254
 3.7. 1T'-MoS_2 as topological insulators 254

* Corresponding author.
E-mail address: jai.bhu@gmail.com (J. Singh).
[1] These authors contributed equally to this work.

https://doi.org/10.1016/j.apmt.2018.09.003
2352-9407/© 2018 Published by Elsevier Ltd.

4. Growth methods 255
4.1. Mechanical exfoliation 255
4.2. Chemical vapor deposition 255
4.2.1. Vapor phase growth 256
4.3. Liquid-phase preparations 257
4.4. MoS_2 film fabricated by RF sputtering 258
4.5. Atomic layer deposition (ALD) 258
5. Applications 260
5.1. TMDCs transistors 260
5.2. Field emission 261
5.3. Photovoltaics and photodetection 261
5.4. Gas sensing 262
5.5. Hydrogen production 262
6. Hydrogen evolution mechanism 264
7. Composites with conductive hosts 265
8. Defective MoS_2 nanosheets and amorphous MoS_2 267
9. Role of the phase, edge, and vacancies 267
10. The photoelectrocatalytic (PEC) HER 267
11. Prospects and direction 267
12. Summary 268
Acknowledgments 268
References 268

1. Introduction

The discovery of graphene in 2004 by Geim & Novoselov as the first two-dimensional (2D) material with excellent electronic, optical and mechanical properties has given birth to research on several other 2D materials [1]. Graphene has been extensively investigated due to its unique features such as high field effect mobility $\sim 10^4$–10^5 $cm^2 V^{-1} s^{-1}$, superior flexibility, better transparency, improved chemical stability, and high surface area [1,2]. Later-on, emerged as a promising candidate for the post-silicon age with numerous technological applications in nanoelectronics, optoelectronics, spintronics, energy harvesting and sensors [2c–e,3]. However, pristine graphene has no band gap, so it is unlikely to be utilized for the fabrication of logical circuits. In this context, 2D materials, especially TMDCs, have gained worldwide attention in recent years for possible application in field-effect transistors (FETs), integrated circuits, photodetectors, memory devices, chemical and biosensors, lithium-ion batteries, hydrogen evolution catalysis, and supercapacitors [3d,e,4,5]. The advantages originate from the high surface-to-volume ratio, unique electrical, mechanical, magnetic, and optical properties. TMDCs are inorganic layered materials exhibiting a variety of electronic features ranging from semi-conductivity to superconductivity making these layered materials potentially useful in next-generation nanoelectronics. Materials such as MoS_2, $MoSe_2$, WS_2, WSe_2, h-BN, Bi_2Te_3, and Bi_2Se_3 have been considered as prospective materials to fabricate nanoelectronic devices due to their properties and ease of fabrication [6]. Recently, Late et al. [7a] reported rapid synthesis and characterization of various other dichalcogenides, i.e., GaS and GaSe using a micromechanical cleavage method and their optical properties. Moreover, single-layer GaS and GaSe nanosheets represent good field effect mobility which can be beneficial for many nanoelectronic devices [7b]. Among all TMDCs, MoS_2 exhibit superior optoelectronic and catalytic properties compared to the conventional semiconductors. It is vital to fabricate transistors based on these materials for benchmarking essential transport characteristics toward possible use in device applications. The monolayers of MoS_2 have a direct band-gap of $\sim$1.8 eV [7,8]. The successful fabrication of FETs with high ON/OFF ratio and NOR logic operation, phototransistors, and gas sensors show the versatility of single layer MoS_2 [8].

Usually, bulk counterparts of the multilayered materials are formed by the weak interaction between the layers, which serves to stabilize the structure. TMDCs (e.g., MoS_2, WS_2, WSe_2, etc.) consist of a sandwich structure in which a layer of transition metal (e.g., Mo, W, Nb) atoms are hexagonally packed between two layers of chalcogen (e.g., S, Se, Te) atom. The intercalation or doping into the interlamellar space of these materials enables scientists to tailor their physical properties. As the number of layers is closely related to the physical properties, thus allowing to tune electrical properties by adjusting the number of layers. With the help of the accumulated synthetic knowledge, there has been particular interest in monolayered materials.

1.1. *Benefits of MoS_2 over Silicon*

TMDCs have certain advantages over silicon (Si) when it comes to creating a microchip for miniaturization. In a 0.65 nm thin sheet of MoS_2, the electrons can move around as quickly as in a 2 nm thick sheet of Si. It is not currently possible to fabricate a layer of silicon as thin as a monolayer MoS_2, so the futuristic chips using MoS_2 will be smaller than state of the art silicon chips. Reduced electricity consumption is another advantage, along with mechanical flexibility. Moreover, the benefit of MoS_2 comes from the fact that it is a 2D material whereas silicon is 3D. MoS_2 seems to be a better alternative than Si for transistors manufacturing. This consents one to foretell size-dependent properties and interchange collaborations for a broad range of semiconductors regardless of their size, shape, composition and synthetic protocol. MoS_2 is also being used in the fabrication of solar cells and LED which leads that this material may have significant future possibilities for various field of electronics and futuristic gadgets.

Present review summarizes the structure and synthesis of mono/few layers of MoS_2 fabricated by numerous techniques such as mechanical and chemical exfoliation, RF-sputtering, atomic layer deposition (ALD) and chemical vapor deposition (CVD), etc. Extensive theoretical aspects combined with the experimental observations to provide more insights on the dielectric and topological behavior of MoS_2 are highlighted. Additionally, broad studies based on potential applications of MoS_2 like FET device, sensor, solar cells, field emission and as a catalyst for hydrogen production by of electrochemical and photoelectrochemical water splitting have been included.

2. Properties of transition metal dichalcogenides

TMDCs with an MX_2 stoichiometry (III-VI group, and IV-VI group compounds) possess similar crystal structure like layered insulator (h-BN); single element materials like black phosphorus (BP), silicene and germanene; V-VI group of topological insulators (TIs) e.g. Bi_2Te_3, Sb_2Se_3 and Bi_2Se_3; transition metal oxides/hydroxides, such as MoO_3, V_2O_5, $Ni(OH)_2$ and others (including metal-organic frames and mica etc.).[8] By chemical compositions, individual layers of bulk TMDCs (MX_2) is supported by a transition metal (M = Mo, W, Ti, etc.) atomic layer sandwiched between two chalcogens (X = S, Se, and Te, etc.) atomic layers.

2.1. Crystal structures

In the present review, the emphasis is on MoS_2, depending on the atomic stacking configurations, the MoS_2 crystal structure can be classified into **4 Polytypes**: **1H, 1T, 2H and 3R** according to a recent report [8g,h]. However, MoS_2 exhibiting three structural polymorphs: **2H**, **3R**, and **1T** (Fig. 1(a)) are well reported [8i,j]. The structural changes directly connected to the physical properties of MoS_2. Naturally occurring bulk MoS_2 possess thermodynamically favored 2H phase with the S-Mo-S layers stacked in hexagonal symmetry. On the other hand, 3R-polytype of MoS_2 shares the MoS_6 with 2H in each single layer with rhombohedral symmetry. The third polytype (1T phase) is metastable (not occurring naturally), however can be obtained in the form of single layer by chemical or electrochemical exfoliation from its bulk counterpart (2H-MoS_2) [8i]. The metastable 1T has one layer per unit cell with Mo atoms in octahedral symmetric arrangement. Because of the metastable nature 1T-MoS_2, can be readily transformed to 2H phase via intralayer atomic gliding under specific conditions [8i]. Naturally occurring 2H-MoS_2 is semiconducting while 1T-MoS_2 is metallic in nature [8a–c]. Fig. 1(b) shows the single-layer MoS_2 crystal structure top and side view [7a].

2.2. Electronic band structures

Recent advancement in nanoscale characterization and device fabrication have opened up new opportunities for 2-D materials providing better insights in structure and their possible applications. Graphene retains remarkable high charge carrier mobility at room temperature, high optical transmittance, and flexibility [1,7e]. The electronic band structure of graphene has a linear dispersion near the K point [8d]. The bulk MoS_2 crystal is built up of van der Waals bonded by S-Mo-S units. Each of these stable units consisting two hexagonal planes of S atoms sandwiching a hexagonal plane of Mo coordinated through ionic-covalent interactions with each other in a trigonal prismatic arrangement as shown in Fig. 2 [9b]. First principles, tight-binding approximations, and many spectroscopy tools showed general electronic feature of many TMDCs having similar band structures [9,10]. In general,

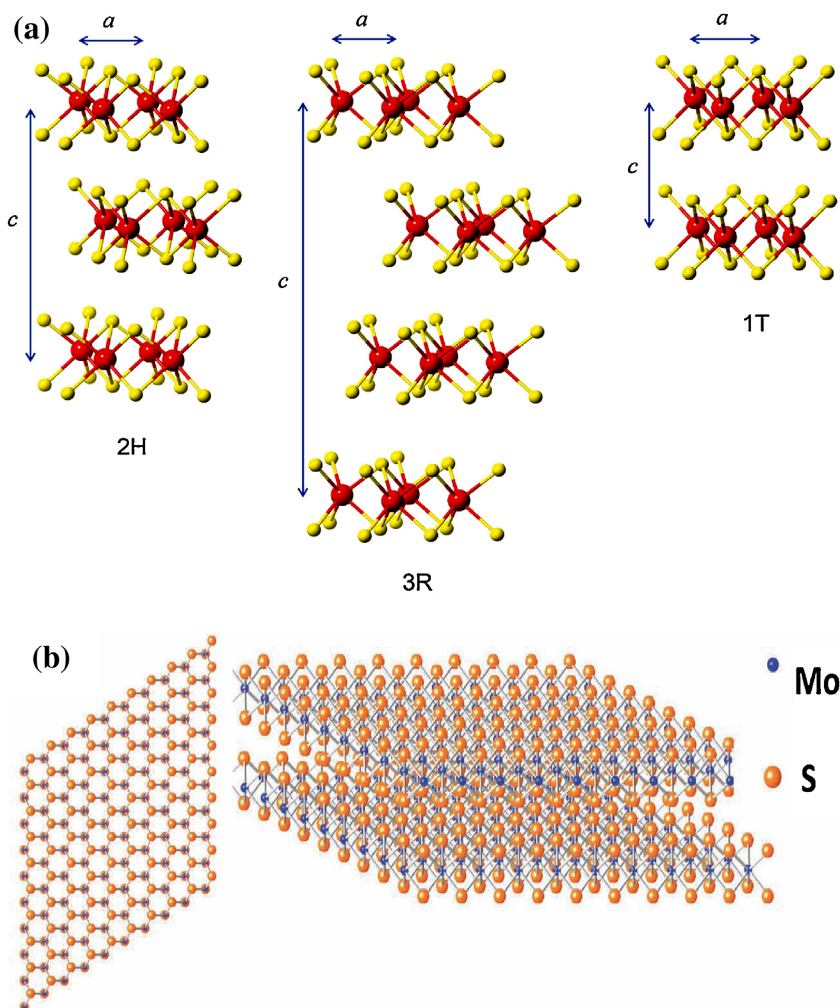

Fig. 1. (a) Crystal structure of MoS_2, 2H (left), 3R (center) and 1T (right) respectively. Atom color: Red, Mo; yellow, S. (*Reproduced with permission from ref. 8(i) Chem 1 (2016) 699–726.*) (b) Single-layer MoS_2 crystal structure top and side view. (*Reproduced with permission from ref. 7(a) Adv. Funct. Mater. 22 (2012) 1894–1905.*)

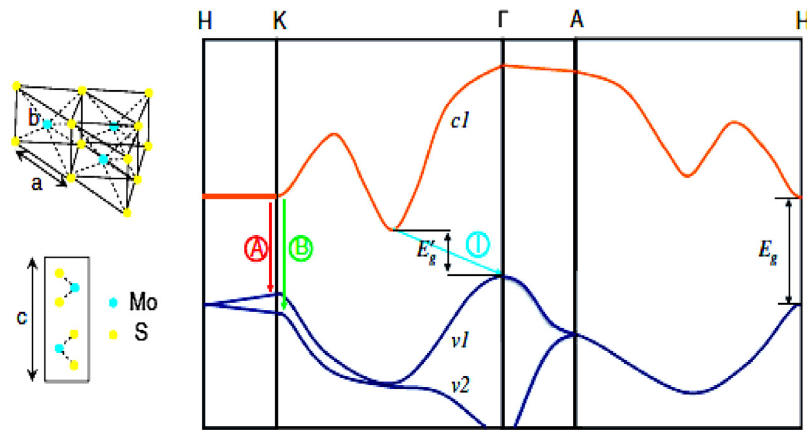

Fig. 2. Lattice structure of MoS_2 in both: in and out-of-plane directions and clear band structure of bulk MoS_2. c1 is showing the lowest conduction band while v1 and v2 the highest split valence bands. A and B represented the direct- gap transitions, and I indicates the indirect-gap transition. E_g' is the indirect band gap for the bulk, and E_g is the direct band gap for the monolayer. (*Reproduced with permission from ref. 9(b) Phys. Rev. Lett. 2010, 105, 136805.*)

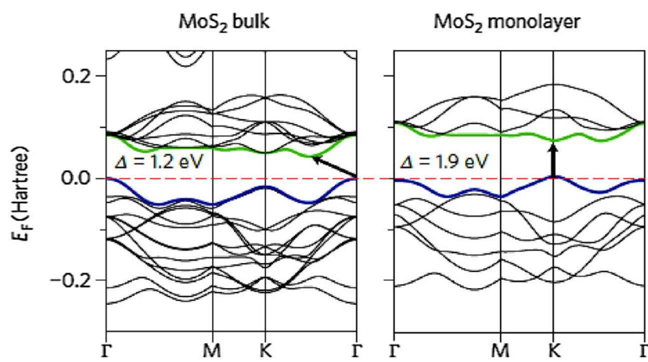

Fig. 3. Band structures for bulk and monolayer MoS_2 calculated from first-principles density functional theory (DFT). The pointer indicates the fundamental bandgap (direct or indirect) and the horizontal dashed lines indicate the Fermi level. The top of the valence band and bottom of the conduction band are highlighted in blue and green color, respectively. (*Reproduced with permission from ref. 9(a) Nature Nanotechnology, 2012, 699.*)

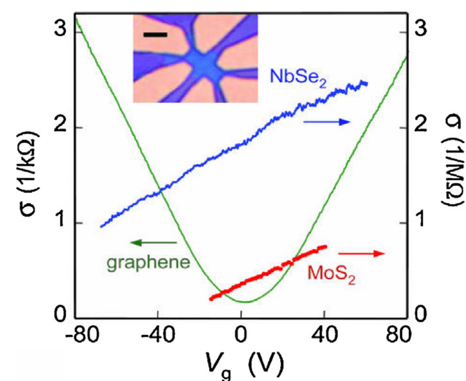

Fig. 4. The variations of electrical conductivity of $NbSe_2$, MoS_2, and graphene as a function of gate voltage at room temperature. The inset shows the typical devices used for such measurements. (*Reproduced with permission from ref. 11(b) Proc. Natl. Acad. Sci. USA, 2005, 102, 10451–1045.*)

MoX_2 and WX_2 compounds are semiconducting whereas NbX_2 and TaX_2 are metallic [9,10]. The band structures calculated from first-principles density functional theory (DFT) for bulk and monolayer MoS_2 are shown in Fig. 3. The band gap transition is indirect for the bulk material at the Γ-point but gradually shifts to be direct for the single layer. Due to quantum confinement effect, change in the band structure with layer number is observed, resulting in a shift in hybridization between p_z orbitals on S atoms and *d* orbitals on Mo atoms [9c,10d]. At the same time the electronic distributions are also spatially correlated to the atomic structure.

For MoS_2, DFT calculations indicate that the energy states of the conduction-band at the K-point are because of localized *d* orbitals on the Mo atoms, located in the middle of the S-Mo-S and relatively unaffected by interlayer coupling [9a]. Conversely, the energy states close to the Γ-point resulting combinations of antibonding pz-orbitals on the S atoms and the *d* orbitals on Mo atoms holding substantial interlayer coupling effect [8e]. Therefore, as the layer numbers change, the direct excitonic states near the K-point are relatively unchanged, however the transition at the Γ-point shift considerably from an indirect to a direct one [9b]. The MoS_2 undergo a similar indirect-to direct band gap transition with decreasing layer numbers. The bandgap varies from energy range 1.1–1.9 eV [9,10]. More detailed theoretical description based on density functional theory (DFT) revealing some intriguing results on the structure and properties of MoS_2 are highlighted in the theoretical aspect section hereafter.

2.3. Electrical and optical properties

The properties of TMDCs are entirely different from graphene. Graphene shows exceptionally high carrier mobility exceeding $10^6\,cm^2\,V^{-1}\,s^{-1}$ at low temperature (2 K) and $10^5\,cm^2\,V^{-1}\,s^{-1}$ at room temperature for devices encapsulated in BN dielectric layers [11a,b]. But, graphene does not have a bandgap so FETs made from graphene cannot be switched efficiently off and having low on/off switching ratios. As already mentioned, the bulk MoS_2 possess an indirect band gap of 1.2 eV, while single-layer MoS_2 is a semiconductor with a direct band gap of 1.8 eV. *K. S. Novoselov et al.* first characterized electrical properties of MoS_2 and compared with other two-dimensional materials as shown in Fig. 4 [11c]. They found the electrical conductivity of MoS_2 ($3\,cm^2\,V^{-1}\,s^{-1}$), was much lesser than graphene.

In FET structure, 2D TMDCs has been used as a semiconducting channel region, which is connected to the source and drain, separated by a dielectric layer from the gate electrode [11c]. The current flowing between the electrodes of origin and drain is controlled by the gate voltage modulating the resistivity of the channel. Silicon is the first material that meets the industrial requirements for performance and manufacturability in digital logic [11c]. The desirable properties of digital logic transistors are high current on/off ratio (the ratio of on-state to off-state conductance) for efficient switching, high charge-carrier mobilities for fast operation, improved conductivity (the product of charge density and mobility) and low off-state conductance. The on/off ratios between 10^4

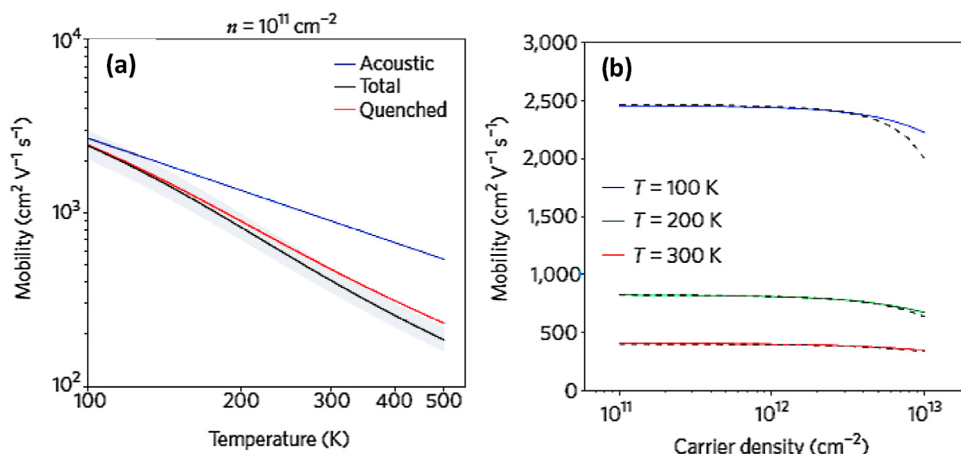

Fig. 5. (a) Carrier mobility calculated from first-principles DFT calculations for the electronic band structure, phonon dispersion and electron-phonon interactions of mono-layer MoS_2 as a function of temperature and. (b) carrier density, In figure (a), the gray band shows the uncertainty in calculated mobility values due to a 10% change in computed deformation potentials associated with phonons. (*Reproduced with permission from ref. 9(a) Nature Nanotechnology, 2012, 699.*)

and 10^7 for the logic circuits are highly desirable. Two-dimensional MoS_2 fulfilled all these criteria because of sizeable bandgap to support high on/off ratios while maintaining high carrier mobilities and scalability to ever-smaller dimensions. The unique properties like excellent mobility and structural stability comparable to Si make MoS_2 an ideal candidate for FETs application [11d]. One of the earliest uses of MoS_2 with back-gated configurations in FETs was reported in 2005, resulting high mobility values in the range 0.1–10 $cm^2\,V^{-1}\,s^{-1}$ [11c]. Recently, *Kis and coworker* reported the implementation of a top-gate transistor based on monolayer MoS_2 [3e]. This device showed n-type conduction, with the room-temperature mobility of >200 $cm^2\,V^{-1}s^{-1}$, excellent on/off current ratio (~10^8), and a subthreshold swing of 74 mV dec^{-1} [3e]. The high-*k* dielectric HfO_2 was used in the device which help to improve the mobility MoS_2 single layer. The top-gated geometry allows a reduction in the voltage necessary to switch the device while permitting the integration of multiple devices on the same substrate. FET fabricated with MoS_2 obtained from liquid exfoliation, and CVD methods show similar electrical performance [11e,12a–c].

MoS_2 not only compete with conventional III–V transistors on mobility values, its attractive electrical performance, relatively high natural abundance and a high degree of electrostatic control makes it a viable for low-power electronic [9a]. The charge transport and carriers scattering for 2D TMDCs are confined to the plane of the material. The mobility of carriers is affected by the following main scattering mechanisms: (i) acoustic and optical phonon-scattering; (ii) Coulomb scattering at charged impurities; (iii) surface interface phonon scattering; and (iv) roughness scattering [9a]. The scattering is also affacted by the thickness of the layer, device temperature, effective mass and density of carrier, electronic and phonon-band structure. It is well known that carrier mobility is increased by phonon scattering with increasing temperature. The temperature-dependent electronic mobility of single-layer MoS_2 calculated from first principles by Kaasbjerg et al. is presented in Fig. 5(a) [12d]. At higher temperatures, the optical while at lower temperatures ($T <$ 100 K) acoustic component dominates. The Coulombic scattering in 2D TMDCs is caused by randomly oriented charged impurities within the layer or on the surfaces and is the dominant scattering at low temperatures. As a result, the mobility is also decreased, so the choice of doping in a particular device can strongly influence its performance. Fig. 5(b) shows the effect of carrier concentration and temperature on the carrier mobility of MoS_2.

The optical properties of MoS_2 are highly intriguing. Recently, Mak et al. investigated optical properties like absorption, PL, and photoconductivity spectroscopy on mono and few-layer MoS_2 samples [9b]. For PL studies, MoS_2 samples were suspended and excited with a CW solid-state laser with an excitation wavelength of 532 nm. Fig. 6(a) shows the measured PL intensity under identical

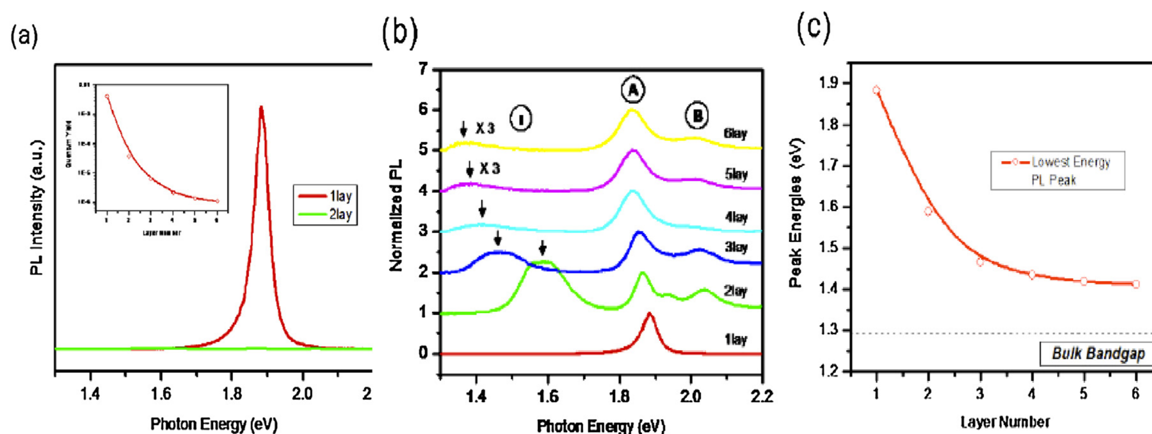

Fig. 6. (a) PL spectra of mono- and bilayer MoS_2 samples. The inset shows the PL QY of thin layers for N = 1–6. (b) Normalized PL spectra by the intensity of the peak of thin layers of MoS_2 for N = 1–6. Intensity for N = 4–6 is magnified, and the spectra displaced for clarity. (c) Band-gap energy of thin layers of MoS_2 as a function of layers. The dashed line shows the (indirect) band-gap energy of bulk MoS_2. (*Reproduced with permission from ref. 9(b) Phys. Rev. Lett. 2010, 105, 136805.*)

excitation at 2.33 eV for a suspended monolayer and a bilayer sample. The PL quantum yield (QY) drops steadily with increasing thickness $N = 1–6$ presented in the inset of Fig. 6(a). A PL QY of the order of 10^{-5} to 10^{-6} was estimated for few-layer samples of $N = 2–6$, a value as high as 4×10^{-3} was observed in the limit of monolayer thickness [9a]. PL for bulk MoS_2 is an elusive phonon-assisted process and is known to have negligible QY, similar to an indirect bandgap material. The normalized PL spectra for mono- and few-layer samples in Fig. 6(b) revealed their discrete nature. The PL spectrum of suspended single-layer MoS_2 samples consists of a single narrow feature of ~50 meV width, centered at 1.90 eV. While few-layer samples exhibit multiple emission peaks (labeled A, B, and I). Peak A coincides with the monolayer emission peak, and shifts to the red side and broadens slightly with increasing layer numbers. The thickness dependent bandgap is shown in Fig. 6(c) [9a].

2.4. Vibrational properties

The vibrational and other physical properties of layered materials (i.e. graphene and TMDCs etc.) are completely distinct than their bulk counterpart. Since vibrational properties are sensitive to thickness, therefore it is necessary to study the material properties with varied thickness. Raman spectroscopy being a fast, nondestructive, high-resolution technique have been employed to determine the number of layers, as well as to examine the thickness dependent properties of various materials [12e,13a,b]. A detailed study conducted by C. Lee et al. had nicely explained how the weak van der Waals-like interlayer interactions affect the interlayer bonding, lattice vibrations and the overall properties of the system [13c]. It is revealed from the study that going from twelve layers to monolayer, MoS_2 exhibits exciting physical properties which are absent in bulk crystal. The optical image of the different MoS_2 layer is shown in Fig. 7, the number of the layers was confirmed by AFM. A Raman spectrum for single- and few-layer MoS_2 illustrated in Fig. 8. Only two, out of four, (E^1_{2g} and A_{1g}) modes near 400 cm^{-1} are observed. The other two modes (E_{1g}, E^2_{2g}) could not be detected either due to selection rules for scattering geometry (E_{1g}) or because of the limited rejection of the scattered Rayleigh radiation (E^2_{2g}) [13b]. Single-layer MoS_2 exhibits a strong in-plane vibrational mode near ~384 cm^{-1} corresponding to the E^1_{2g} mode. Some report claims the similar observations with different laser wavelength [13d,e]. Lee et al. reported that the E^1_{2g} vibration shifted toward lower wave number (redshifts), while the A_{1g} to upper wave number (blue shifts) with increasing sample thickness [13c,14a]. The observed upper shift of A_{1g} peak with increasing layer number is consistent with the predicted stiffening, while the behavior of the E^1_{2g} mode doesn't. This conflicting result could reveal the presence of additional interlayer interactions; which also indicate that the implicit assumption of stacking affecting the intralayer bonding is incorrect. It is monotonic as a function of film thickness (Fig. 8b). Raman mapping for the E^1_{2g} and A_{1g} mode show these opposing shifts with layer thickness as presented in Fig. 8(c) and (d), respectively [13b]. For four or more layer system, the frequencies of both modes tend to the bulk values [13b]. The aforemention observations suggest that the Van der Waals force play a trivial role on stacking of MoS_2 [13b]. A detail on position of different corresponding frequencies of E^1_{2g}, and A_{1g} peak examined using different laser lines are provided in Table 1 [13c].

2.5. Mechanical properties

MoS_2 could be a promising material for next-generation flexible electronic devices. The mechanical properties of single-layer MoS_2 were first reported by Bertolazzi et al. [14a]. Bertolazzi and co-worker mechanically exfoliate single and bilayer MoS_2 from bulk and transferred to a substrate with an array of microfabricated circular holes as shown in Fig. 9. The Mechanical properties of the

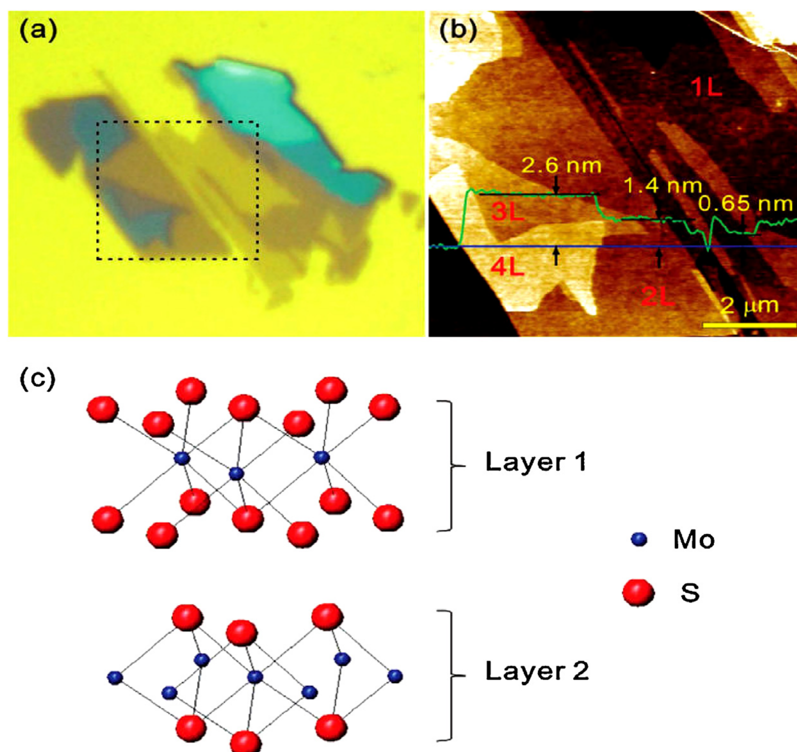

Fig. 7. (a) Optical image of MoS_2 layers deposited on the SiO_2/Si substrate. (b) AFM height indicated by dotted lines in (a). The thickness of each layer is taken along the blue line in the AFM image and height profile is shown by a green line. (c) Schematic structure of the MoS_2 bilayer. (*Reproduced with permission from ref. 13(b) ACS Nano, 2010, 4, 2695–2700.*)

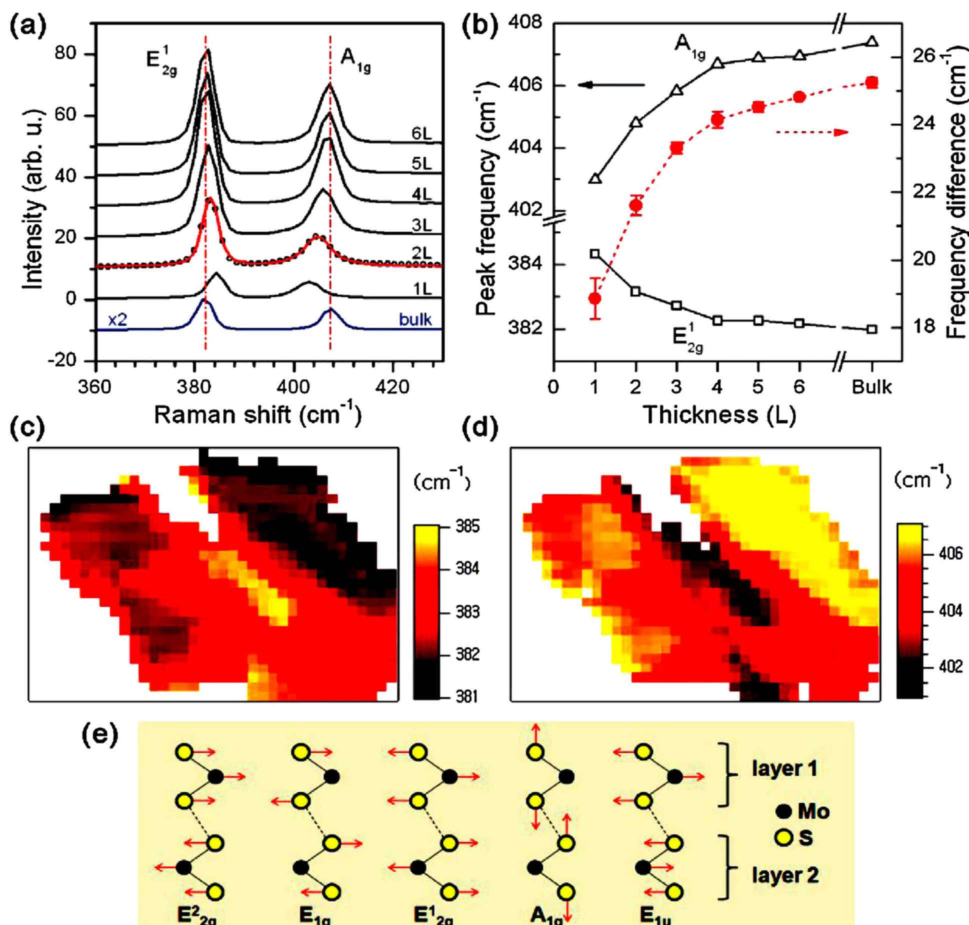

Fig. 8. (a) Raman spectra of thin and bulk MoS_2 samples. The solid line for the 2L spectrum represents a double Voigt fit through data (circles for 2L, solid lines for the rest). (b) Frequencies of $E^1{}_{2g}$ and A_{1g} Raman modes (left vertical axis) and their difference (right vertical axis) as a function of layer thickness. (c, d) Spatial maps of the Raman frequency of $E^1{}_{2g}$ (c) and A_{1g} modes (d) for the sample in (e) Atomic displacements of the four Raman-active modes and one IR-active mode (E_{1u}) in the unit cell of the bulk MoS_2 crystal as viewed along the [1000] direction. (*Reproduced with permission from ref. 13(b)* ACS Nano, *2010, 4, 2695–2700.*)

Table 1
Summary of the $E^1{}_{2g}$ and A_{1g} peak frequencies with various laser lines "1L", "2L", "3L", and "4L", indicate monolayer, bilayer, trilayer, and four layers, respectively. A single data represents the average value from three different samples. The measurement results with 514.5 nm line are extracted from reference [3(e)]. Ref 13(c) Adv. Funct. Mater. 2012, 22, 1385–1390.

Laser lines [nm]	$E^1{}_{2g}$ peak frequency [cm^{-1}]					A_{1g} peak frequency [cm^{-1}]				
	1L	2L	3L	4L	Bulk	1L	2L	3L	4L	Bulk
325	384.2	382.8	382.8	382.7	382.5	404.9	405.5	406.3	407	407.8
488	384.7	383.3	383.2	382.9	383	402.8	405.5	406.5	407.4	408
514.5 [15]	384.3	383.2	382.7	382.7	382	403	404.8	405.8	406.7	407.5
532	384.7	382.5	382.4	382.4	383	402.7	404.9	405.7	406.7	407.8
632.8	385	383.8	383.8	382.9	381.5	403.8	404.8	405	406	406.6

suspended, free-standing membranes were probed with indentation experiments using an atomic force microscope (AFM) with a standard silicon cantilever (Fig. 9(c)). Bertolazzi et al. found that the in-plane stiffness of monolayer MoS_2 is $180 \pm 60\,Nm^{-1}$, corresponding to an effective Young's modulus of 270 ± 100 GPa. These values are comparable to steel.

The force–deflection curves for mono- and bilayer MoS_2 are shown in Fig. 10. Furthermore, Bertolazzi et al. extracted the pretension $\sigma_0{}^{2D}$ and the membrane elastic modulus E^{2D} from a least-squares fit of the experimental curves with the Eq. (1)

$$F = \sigma_0^{2D}\pi\delta + E^{2D}\frac{q^3\delta^3}{r^2} \tag{1}$$

Calculating these parameters for a total of nine monolayers samples and averaged for the elastic modulus E^{2D} of 180 ± 60 Nm^{-1} as shown in the left panel of Fig. 11. The pre-stress $\sigma_0{}^{2D}$ is in the range of 0.02 to 0.1 Nm^{-1}. The Young's modulus was found to be $E_{Young} = 270 \pm 100$ GPa by assuming the thickness of monolayer is 0.65 nm. The Young's modulus of bilayer MoS_2 was obtained ~200 ± 60 GPa. The average of maximum stress for single and bilayer MoS_2 membranes were found to be 15 ± 3 and $28 \pm 8\,Nm^{-1}$, respectively (Fig. 12). The lower value of Young's modulus for bilayer MoS_2 may be due to defects or interlayer sliding.

Gomez et al. measured the mechanical properties of few layers (5–7 layers) MoS_2 similarly as disused for single and bilayer MoS_2 [14c] and shown in Fig. 12(a). Fig. 12(b) shows typical force vs. deformation traces ($F(\delta)$ traces measured at the center of the suspended part of MoS_2 layers), and the shape of the traces indicate its thickness dependent. The thinnest sheets (5–8 layers) shows

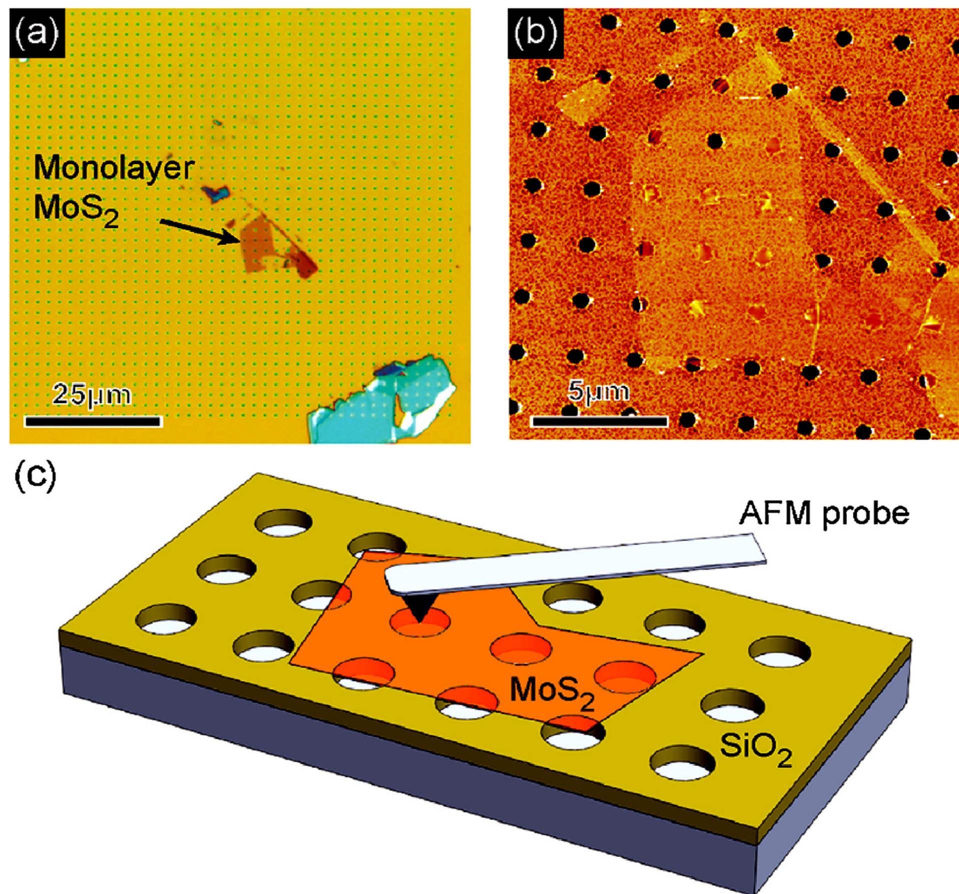

Fig. 9. (a) The Optical image of a single layer MoS_2 flake transferred onto the pre-patterned SiO_2 substrate containing an array of circular holes of diameter 550 nm. (b) AFM image of the same monolayer MoS_2. (c) Schematic illustration of the indentation experiment. The AFM tip is placed above the center during measurements and slowly lowered while monitoring its deflection. (*Reproduced with permission from ref. 14(a) ACS Nano, 2011, 5, 9703–9709.*)

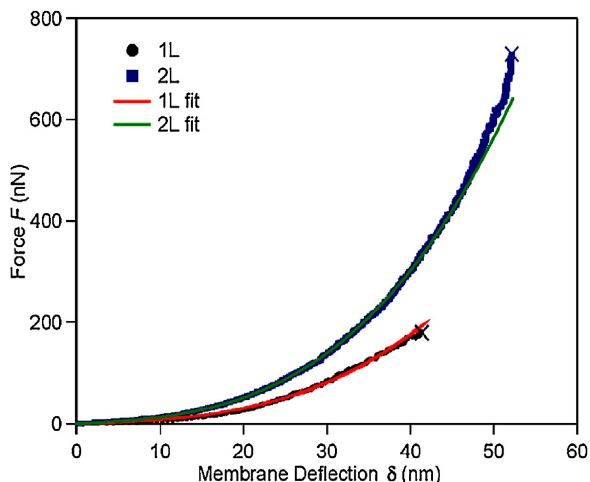

Fig. 10. The loading curves for single and bilayer MoS_2 and the least-squares fit of the experimental indentation curves to Eq. (1). The symbol × marked the fracture point of the Membranes. (*Reproduced with permission from ref. 14(a) ACS Nano, 2011, 5, 9703–9709.*)

the strongly nonlinear $F(\delta)$ curve, while sheets thicker than ten layers $F(\delta)$ traces are linear [14c]. Young's modulus (E) and the initial pretension (T) of suspended MoS_2 nanosheets (thin layer) extracted from the non-linear $F(\delta)$ curve. E = 0.35 ± 0.03 TPa and T = 0.05 ± 0.02 Nm^{-1} was calculated for 8 layer from $F(\delta)$ curve as shown in Fig. 13(a). Gomez et al. also calculated E and T for thicker films Fig. 13(a) [14c]. The histogram of the pre-tension and Young's modulus were obtained for 13 membranes 5–10 layers thick by fitting the force vs. deformation traces to Equation 2 and shown in Fig. 13(c) and (d).

$$F = \left[\frac{4\pi E}{3(1-\nu^2)}\left(\frac{t^3}{R^2}\right)\right]\delta + (\pi T)\,\delta + \left(\frac{q^3 E t}{R^2}\right)\delta^3 \tag{2}$$

The strength of individual single layer MoS_2 is between 6 and 11% of their Young's modulus, and it also reflects the inherent strength of interatomic bondings [14c]. Bertolazzi et al. also compared these values to several other common engineering materials as presented in Table 2 and found that the strength of single-layer MoS_2 was exceeded only by carbon nanotubes and graphene [14a]. MoS_2 has a lower Young's modulus and strength than graphene. The mechanical properties of MoS_2 layers indicate that MoS_2 could be suitable for integration in flexible electronic circuits.

3. Theoretical aspects

3.1. *First principles perspective of MoS_2*

Computer simulations are emerging as a bridge between experiment and theory. In particular, simulations based on first principles methods play a crucial role, because they not only help to explain experimental results but also can predict properties of new materials or new structures with high accuracy [15a,b]. High-level density functional theory (DFT) calculations have emerged as a robust approach toward mechanistic insights into the properties of 2D materials. The growth of ab-initio based physics is the outcome

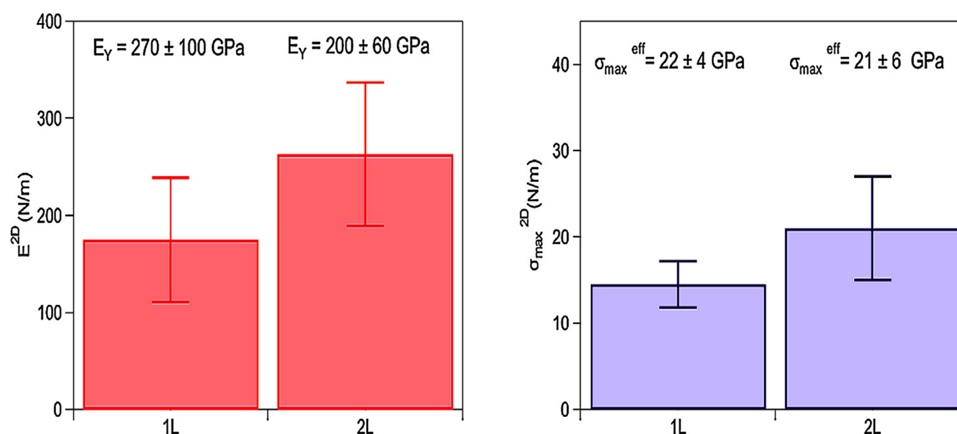

Fig. 11. Young's modulus E^{2D} (left) and maximum breaking stress σ-max 2D at the central point (right) of the film for single and bilayer MoS_2 flakes extracted from the experimental data. (*Reproduced with permission from ref. 14(a) ACS Nano, 2011, 5, 9703–9709.*)

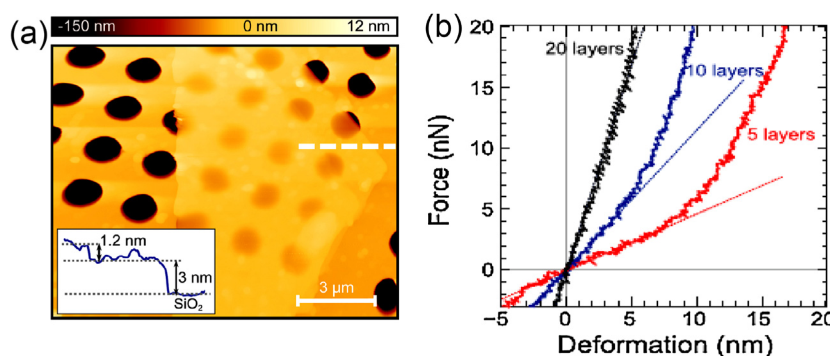

Fig. 12. (a) Topography AFM image of a 3–4.2-nm-thick (5–7 layers) MoS_2 flake deposited on SiO_2/Si substrate pre-patterned with an array of holes 1.1 μm in diameter. Inset image shows line profile acquired along the dashed line, (b) Force versus deformation curve measured at the center of the suspended part of MoS_2 nanosheets with 5, 10, and 20 layers. The slope of the curve around zero deformation is plotted as a dotted line. (*Reproduced with permission from ref. 14(c) Advanced Materials, 24, 6, 772–775 (2012).*)

of the rapid development of computer technology. Given the crystalline atomic structures, the DFT method is capable of predicting the electronic, magnetic, and optoelectronic properties [15c]. One of the exciting example is the discovery of topological materials aided by computational design from first principles [15d]. The first-principles computational design approaches have worked out as a powerful research tool in realizing theoretical models of various phases in real materials systems, outputting relevant properties that can be tested and confirmed directly by the experiments.

3.2. Background

A detailed description of the quantum mechanical behavior of atoms requires explicit consideration of interactions between electrons and nuclei. The Born–Oppenheimer approximation is the initial approximation used to solve the Hamiltonian by because the nuclei cannot move as much as electron due to its massive mass. As a result, the motions of the two subsystems (electrons and nuclei) can be uncoupled. Thus the Hamiltonian for given N electrons moving in the external potential (V_{ext}) of fixed nuclei in atomic units $\hbar = m = |e| = 1$ becomes [16a]:

$$H = -\frac{1}{2}\sum_i \nabla_i^2 + \sum_i V_{ext}(r_i) + \frac{1}{2}\sum_{ij}^{i} \frac{1}{r_{ij}} \quad (3)$$

An analytic solution of this many-body Schrodinger equation is impossible to obtain because of 3N degree of freedom for each electron.

The most popular method for addressing the problem is the application of density functional theory (DFT) which was developed by Hohenberg, Kohn, and Sham and is based on the electronic density distribution $\rho(r)$ rather than the many-electron wave function. Kohn-Sham (KS) theory is based on a basic ansatz, namely that the ground state density, $\rho(r)$, of an interacting system is also the ground state density of a non-interacting system with an efficient potential $V_{eff}(r)$. The electron density is, therefore, determined from a single-particle Schrodinger equation [16a]:

$$\left[-\frac{1}{2}\nabla^2 + V_{eff}(r)\right]\phi_i(r) = \varepsilon_i \phi_i(r) \quad (4)$$

where $\phi_i(r)$ are the single electron KS orbitals giving the density: $\rho(r) = \sum_i |\phi_i(r)|^2$, where the sum is over the occupied states. The effective potential $V_{eff}(r)$ is given by where $V_{ext}(r)$, E_H and E_{XC} represent the Coulomb interaction between electrons and ions, Coulomb interaction among the electrons and exchange-correlation interaction, respectively. The effective potential depends on the electron density that is determined by the Kohn-Sham orbitals, which in turns depends on the effective potential. Thus the problem of solving the Kohn-Sham equation is iterative with the requirement that the effective potential and the resulting charge density are self-consistent. The validity of effective implementation of the Kohn-Sham method lies in finding a good approximation for E_{XC} and hence V_{eff} [15a,16a]. The simplest approach is the local density approximation (LDA) where the contribution of each volume element to the total exchange-correlation energy is taken to be that of an element of a homogeneous electron gas with the density corresponding to that point. One strategy to improve the LDA is to

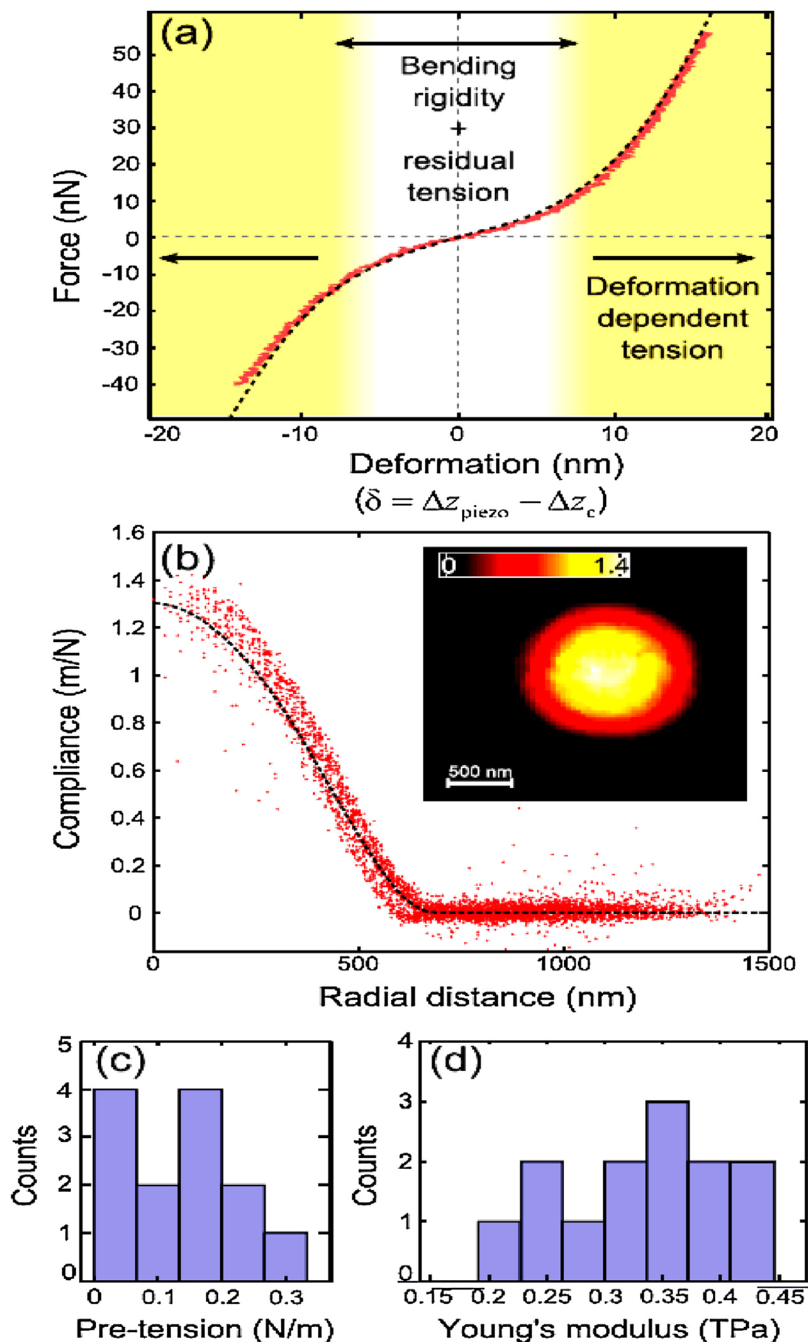

Fig. 13. (a) Force versus deformation curve for eight layers thick suspended MoS_2 over a hole 1.1 μm in diameter. The dotted black trace is the fit to Eq. (2), employed to obtain the Young modulus $E = 0.35 \pm 0.02$ Tpa and the pre-tension $T = 0.05 \pm 0.02$ N m^{-1}. (b) Force–volume measurement is showing a color map of the compliance (inset) and its radially-averaged profile of the sheet. (c) Histogram of the initial pre-tension obtained with the help expression (2) for 13 sheets 5 to 10 layers thick MoS_2. (d) Histogram of Young's modulus obtained from fitting *F(d)* curves to expression (2) for the same 13 sheets plotted in the panel. (*Reproduced with permission from ref. 14(c) Advanced Materials, 24, 6, 772–775 (2012).*)

include the gradient of the charge density in exchange-correlation functional, which is given in generalized gradient approximation (GGA) [15a,16a].

Also, for a crystalline solid, the Bloch theorem can be used to impose boundary conditions for given external potential and electron wave function, resulting in a set of coupled second-order differential equation, each describing an electron moving in an average potential due to the other electrons [16b]. This set of the equation can be for solid-state systems can be solved using localized atomic orbitals or plane-wave expansion of the wave function and k-point sampling in reciprocal space. Depending upon different basis sets many simulation packages like VASP, SIESTA, CASTEP, etc. have been developed to solve Kohn-Sham equations. Usually, valence electrons determine the physical properties of a solid. Therefore, the pseudopotential approximation can be introduced, which removes the core electrons and replaces the strong nuclear potential with a weaker pseudopotential [15a,b].

3.3. Electronic structure of MoS_2 as a function of layers thickness

Electronic structure of bulk MoS_2 finds it as an indirect-band-gap-semiconductor [17a–d]. DFT calculations have shown that

Table 2
Comparison of Young's moduli and breaking strengths for several engineering materials including monolayer MoS_2 [4d,5d,8a,e,9d-e,10a-c].

Material	Young's modulus E_{young} (GPa)	Breaking strength $\sigma_{max}{}^{eff}$ (GPa)	Breaking strength (%) Young's modulus
Stainless steelASTM-A514	205	0.9	0.4
Molybdenum	329	0.5–1.2	0.15–0.36
Polyimide	2.5	0.231	9
PDMS	0.3–0.87	2.24	2.5
Kevlar 49	112	3	2.6
Monolayer MoS_2	270	16–30	6–11
Bulk MoS_2	238		
WS_2 nanotubes	152	3.7–16.3	2.4–10
Carbon nanotubes	1000	11–63	1.1–6.3
Graphene	1000	130	13

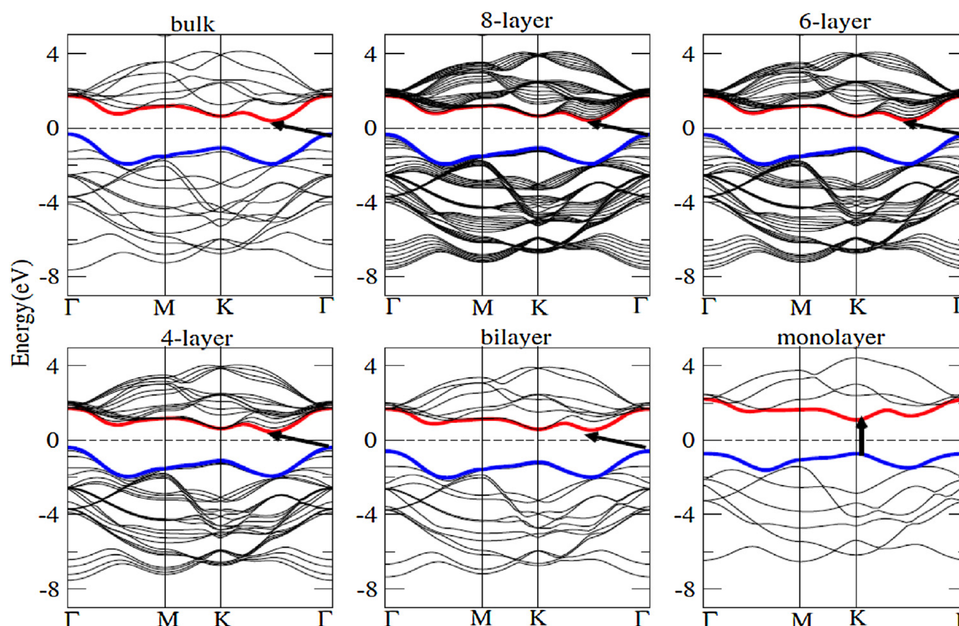

Fig. 14. Electronic band structure of bulk MoS_2, its mono, and multilayers. The top of the valence band (blue) and bottom of the conduction band (red) are highlighted. The arrow indicates the smallest value of the indirect or direct band gap. The Fermi level is set at 0 eV. (*Reproduced with permission from ref. 17, Eur. Phys. J. B., 2012,* ***85****, 186.*)

when MoS_2 is thinned to a single layer, an indirect to direct band gap transition occurs [17a–c]. While downsizing the layers from bulk to the single layer limit, the indirect bandgap increases and becomes more substantial for the monolayers that the materials converted to direct-band-gap semiconductor (Fig. 14), thereby, causing a gradual blue shift (1.14 eV) in indirect band gap energy [17c]. At the same time, magnitudes of the blue shift in the direct bandgap energies at the 'K' point is found to be 0.19 eV. Therefore, the change in the indirect bandgap energy is significantly enhanced than that of the direct band gap energy. The blue shift in the band gap energies is maximum when one goes from bilayer to the monolayer of MoS_2. The conduction band states at 'K' point are mainly due to the localized' orbitals of the Mo atoms, sandwiched between two "S" layers ("S-Mo-S") and relatively unaffected by interlayer coupling. However, the states near the 'Γ' point are due to the combinations of antibonding p_z orbitals of S atoms and the d orbitals of Mo atoms and have a strong interlayer coupling effect [17e]. Therefore, as the layer number changes, the direct excitonic states near the *k*-point are relatively unchanged, but the transition at the 'Γ' point shifts significantly from indirect one to a larger, direct one. Therefore, the change in the band structure with layer number is due to quantum confinement and the resulting change in hybridization between the p_z orbitals on S atoms and d orbitals on Mo atoms. This, indirect-to-direct band gap transition in MoS_2 has opened up a way for potential applications in photonics, optoelectronics, and sensing [17f].

3.4. Dielectric response of MoS_2: electron energy loss spectroscopy

Electron energy loss spectroscopy has been suggested as a powerful technique to identify the number of layers in commercially produced large and uniform 2D sheets [18a]. Electron energy loss spectra (EELS) can also give information about the single electron interband transitions which can be identified in the lower energy side from the collective plasma oscillations [18b]. Theoretical EELS can be calculated from a dielectric function using the expression:

$$Im\left\{\frac{-1}{\varepsilon(\omega)}\right\} = \frac{\varepsilon_2(\omega)}{\varepsilon_1^2(\omega)+\varepsilon_2^2(\omega)} \quad (5)$$

where ε_1, ε_2 are real and imaginary parts of the dielectric function. Note that imaginary part of the dielectric function (ε_2) can be obtained by first-order time-dependent perturbation theory using ground state DFT eigenvalues and eigenfunctions [18c]. The real component of the dielectric function (ε_1) can easily be obtained from ε_2 using Kramers–Kronig relation. The calculated EELS for MoS_2 consists of two prominent resonance features for in-plane polarization ($E\perp c$) that lies (i) below 10 eV which is due to π-plasmons (π-π* transitions) and (ii) above 10 eV which is due to π+σ plasmons (π-σ* and σ-σ* transitions) [Fig. 15(a)], whereas for out-of-plane polarization ($E \parallel c$) only one resonance feature above 10 eV due to π-σ* and σ-σ* transitions, is prominent [18d]. In MoS_2

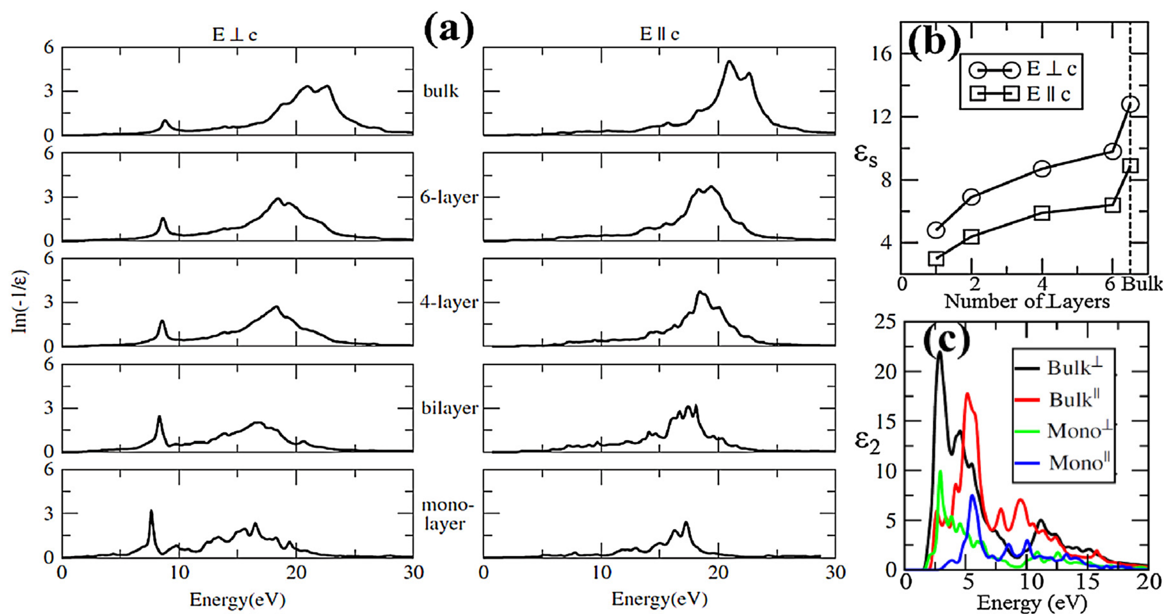

Fig. 15. (a) EELS of MoS2 for E⊥c and E||c with some layers. (b) The variation in the ε_s concerning some layers for both E⊥c and E||c. (c) The imaginary (ε_2) of the dielectric function for bulk and monolayer MoS_2 for both E⊥c and E||c. (*Reproduced with permission from ref. [18(d)], Physica B., 2012, 407, 4627–4634.*)

with 18 valence electrons, the strong covalent bonding between the atoms of Mo and S is made up of 12 electrons per molecule having mixed *s*, *p* and *d* orbitals which results into the σ valence band and the remaining six electrons are responsible for the π-plasmon band [18b]. Among the six electrons in the π-plasmon band, two occupy the $d_z{}^2$ orbitals of the metal atom.

It is found that the π+σ plasmons peak for both perpendicular and parallel polarization remains broad. The loss spectra shift toward lower energies even by the variation of slab thickness from bilayer to monolayer [18d,e]. Π-plasmon peaks shift marginally, but prominent redshift can be seen in π+σ plasmon peaks for both perpendicular and parallel polarization as one goes from bulk to monolayer limit. It emerges that ongoing from bulk to the monolayer, the average concentration of electrons decreases which result into a considerable enhancement in the effective mass of electrons and hence a lower value of ω_p for monolayers, which is consistent with the equation: $\omega_p^2 = \frac{Ne^2}{\varepsilon_0 m_{eff}}$, where N, ε_0, e, and $m_{\rm eff}$ are number density of electrons, permittivthe ity of the free space, charge onthe the electrons and effective mass of the electrons, respectively. Note that experimental EELS of MoS_2 also show keen sensitivity to the number of layers [18f]. Therefore, EELS can be used as a technique to identify the number of layers in 2D sheets of MoS_2.

Static dielectric constant (ε_s) is an essential parameter for device modeling which can be obtained from a real part of dielectric function at zero frequency. A pronounced red shift in the value of ε_s has been reported for both perpendicular and parallel polarization when MoS_2 is thinned to monolayer limit [Fig. 15(b)]. The redshift in the values of ε_s for both the polarization is consistent with the corresponding blue shift in the band gap energies as going from bulk to monolayer limit (Fig. 14) which can be verified from the two band model proposed by Penn for semiconductors [18g]: $\varepsilon_s \approx 1 + \left(\frac{\hbar\omega_p}{E_g}\right)^2$, where ω_p is plasmonic frequency, and is the band gap of given the semiconductor. The imaginary part of the dielectric function (ε_2) that reveals the interband transitions [17d] is highly anisotropic in low energy range and become isotropic in high energy range [Fig. 15(c)]. ε_2 for MoS_2 as a function of layer number remains nearly unchanged regarding peak shift which is understood from the corresponding electronic band structures, where bands above and below the Fermi level resides almost constant that results into virtually no change in the interband transition peaks in ε_2. However, the intensity of the interband transition peaks in the ε_2 decreases significantly which is attributed to reduced in the number of bands (Fig. 14) for transition when the thickness of MoS_2 is diminished to the monolayer.

3.5. A topological aspect of MoS_2

The discoveries of novel materials often drive the progress in materials science. In this regard materials presenting unique quantum mechanical properties are of particular importance. The quantum Hall (QH) state discovered in 1980 [19a] is the first example of a quantum state that does not have spontaneously broken symmetry, which was topologically distinct from all previously known states of matter. Later on, in 1982, the concept of topological description was used to explain the quantization of the Hall conductance in two dimensional (2D) electron gases, which gives rise to a critical characteristic is known as Thouless-Kohmoto-Nightingale-Nijs (TKNN) number that is topologically invariant [19b]. To realize quantum Hall effect (QHE) of materials, a strong external magnetic field is required. Consequently, an alternative theoretical model was proposed by Haldane for 2D honeycomb-lattice [19c]. The Haldane model was further modified by Kane and Mele [19d] which reveals that the intrinsic spin-orbit coupling (SOC) induces novel gapless edge states that counter-propagate at the boundaries with opposite spins, and are protected by time-reversal symmetry (TRS) [19e], resulting in a vanishing charge Hall conductance but nonzero quantum spin Hall (QSH) conductance. This new phenomenon was termed as the QSH effect with the electronic spin as the quantum number and characterized by the Z_2 topological order [19f]. The successful predictions of new topological insulator (TI) materials are perhaps the most spectacular triumph of the modern state-of-the-art first-principles theory that has emerged as a vital tool to enable materials discovery by designing unknown materials as well as unexplored properties of existing materials that are subsequently confirmed by experiments. To date, most TIs are first theoretically predicted or computationally developed, followed by experimental confirmation [15d,19g]. Topological insulators (TIs) materials remain a topic of hot discussion among the researchers in the recent time. The 2016 noble prize in Physics has been awarded

for the "*theoretical discoveries of topological phase transitions and topological phases of matter*."

3.6. Topological Z_2 invariant

The more general mechanism for generating TIs is through an electronic band inversion, where the usual ordering of the conduction and valence band with different parities is 'inverted' by strong SOC effect [20a], thereby, allowing the presence of 2D TI states in a much larger variety of materials. The topological order of electronic band structure, the, i.e., the Z_2 invariant is an important parameter to describe the unique phase of matter [20b]. Among the various computation of Z_2 topological invariants, the Fu-Kane criterion [20c] is exceptionally well suited for analyzing the band structures of 2D crystals. The Fu-Kane approach connects the Z_2 invariants to the matrix elements of Bloch wave functions at time-reversal invariant momentum (TRIM) points in the Brillouin zone (BZ). Note that there are four TRIM points in 2D BZ and time-reversal symmetry (TRS) yields one unique Z_2 invariant, ν, which is given by:

$$(-1)^{\nu} = \prod_{i=1}^{n} \delta_i \quad (6)$$

where $n = 4$ for 2D lattice and δ_i denotes the Pfaffian of a unitary matrix over TRIM points in BZ [20c]. In a crystal with inversion symmetry, Bloch wave functions are also eigenfunctions of the parity operator with eigenvalues $\zeta_m = \pm 1$, and the formula for δ_i simplifies as:

$$\delta_i = \prod_{m} \zeta_m \quad (7)$$

where the product is over the pair, the parities of occupied Kramer's doublet resulting from time-reversal symmetry at the TRIM points without multiplying the corresponding time-reversal partners. Therefore, using above criterion, $\nu = 1$ at a particular TRIM point indicates the non-trivial TI or quantum spin Hall (QSH) state, whereas if the computation with including spin-orbit coupling (SOC) effect yield $\nu = 0$ or trivial state, then there is a band inversion at that particular TRIM point which is accompanied by a change in the parity of two states involved and thus changes the value of ν [20d].

3.7. 1T'-MoS_2 as topological insulators

Monolayer MoS_2 possess a variety of polymorphs such as 1H, 1T and 1T' [Fig. 16(a)]. The most studied 1H structure is a triatomic layer sandwich of Bernal (ABA) stacking with P6−m2 space group, whereas, the three atomic planes in the 1T structure form rhombohedral (ABC) stacking with P3−m2 space group. It has been shown that the 1T structure of MoS_2 is unstable in free-standing condition and undergoes a spontaneous lattice distortion in the x-direction to form a period-doubling 2×1 distorted structure, i.e., the 1T' structure [21a], consisting of 1D zigzag chains along the y-direction [Fig. 16(a)]. Unlike 1T-counterpart of MoS_2, 1T'-MoS_2 is a semiconductor with a fundamental gap (E_g) of about 0.08 eV, located at 'Γ' point [Fig. 16(b)].

The conduction and valence bands undergo a band inversion with a sizeable inverted gap (2δ) of about 0.6 eV at 'Γ' point of 2D Brillouin zone [Fig. 16(b) & (c)]. Note that 1T' structure has inversion symmetry with $Z_2 = 1$ indicating that 2D 1T'-MoS_2 possess QSH insulator phase [21b]. Looking at the orbitals character of inverted band structure near 'Γ,' it was found that the valence band mainly consists of Mo d-orbitals whereas in conduction band S p-orbitals dominate [Fig. 16(b)]. The unexpected band inversion is attributed to the doubling of the Mo chain in the 1T′ structure, which lowers the Mo d-orbitals below p-orbitals of S-atom around 'Γ' point. In the absence of spin-orbit coupling (SOC), this band inversion leads to the appearance of two Dirac cones around 'Γ', whereas SOC opens up a fundamental gap of 0.08 eV at the Dirac points [inset of

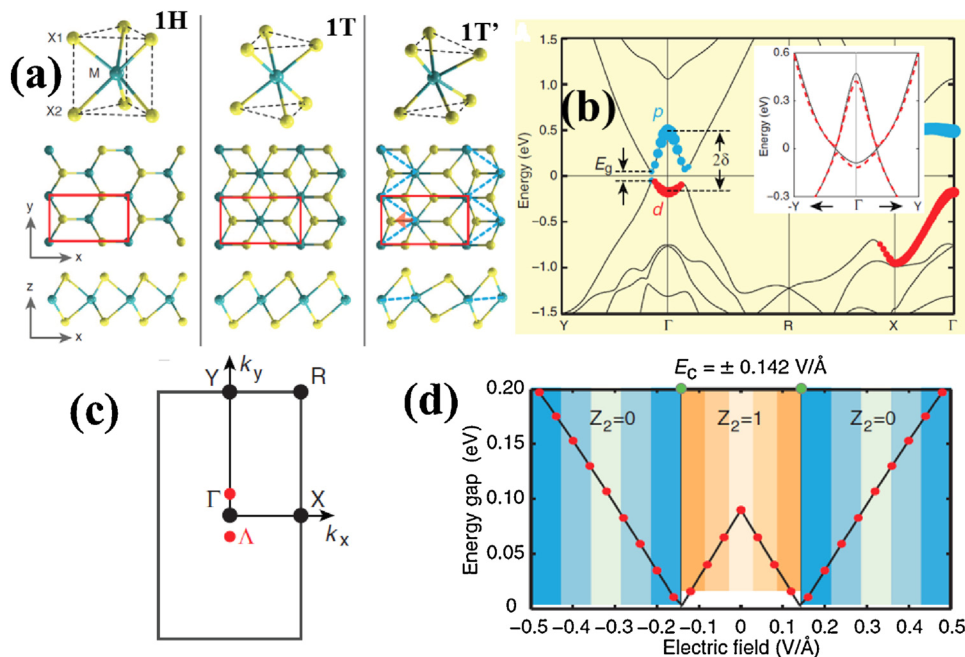

Fig. 16. (a) Atomistic structure of three polymorphs of the MoS_2 monolayer. M stands for metal (Mo), and X stands for chalcogen (S). 1H-MoS_2 and 1T-MoS_2 from ABA and ABC stacking, respectively. 1T′-MoS_2 is distorted 1T-MoS_2 structure where the distorted Mo atoms form 1D zigzag chains indicated by the dashed blue line. Red rectangles show the unit cell. (b) Calculated electronic band structure of 1T'-MoS_2. E_g is a fundamental gap, and 2δ is an inverted gap. The inset compares band structures with (red dashed line) and without (solid black line) spin-orbit coupling. (c) Brillouin zone of 1T′-MoS_2. Black dots marked four time-reversal invariant moments and labeled as Γ, X, Y, and R. Red dots mark the locations of the fundamental gap. (d) Topological phase diagram of 1T′-MoS_2 as a function of the vertical electric field. The critical field strength is ±0.142 V/Å, marked by two green dots. (*Reproduced with permission from ref. [21(b)], Science, 2014 346, 1344.*)

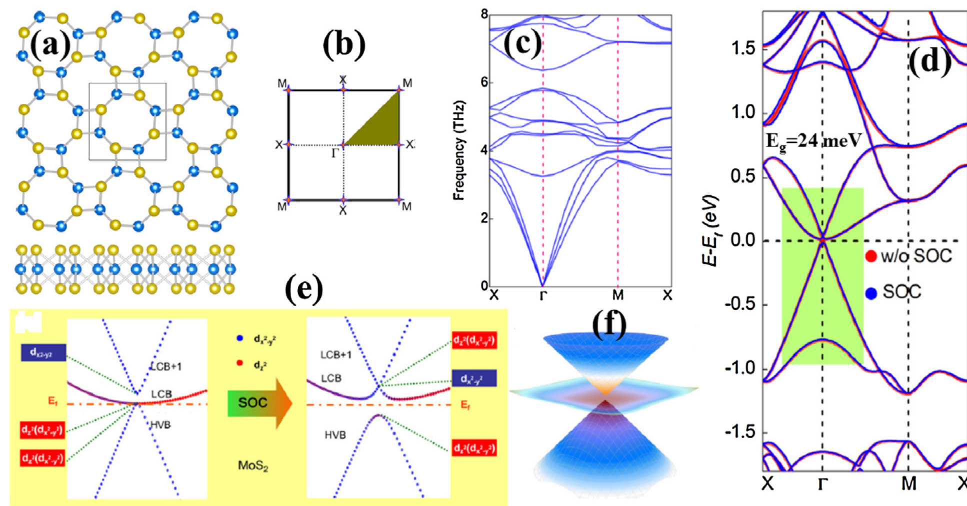

Fig. 17. (a) Top and side view of the crystal structures of monolayer 1S-MoS_2. (b) 2D Brillouin zone of monolayer 1S-MoS_2 (c) Phonon band dispersion of 1S-MoS_2. (d) Electronic band structures of monolayer 1S-MoS_2 with and without spin-orbit coupling (SOC). The Fermi level is set to zero. (e) The evolution of orbitals-resolved band structures of 1S-MoS_2 under SOC effect. (f) Band structure of 1S-MoS_2 around the Fermi level in 2D k-space with energy as the third dimension. (*Reproduced with permission from ref. [22(c)], Phys. Rev. B., 2015, 92, 085427.*)

Fig. 16(b)], that results in QSH transitions by the similar mechanism as the Kane-Mele model for graphene [19d].

The inverted bands between p orbitals of S and d orbitals of Mo located on well-separated atomic planes offer a simple mechanism to control topological electronic properties by perpendicular electric field [21b], which is highly desirable for devices based on van der Waals heterostructures. The vertical electric field induces a topological phase transition [Fig. 16(d)] by breaking inversion symmetry in 1T'-MoS_2 that introduces a substantial Rashba splitting of the doubly degenerate bands near the fundamental gap. On increasing the perpendicular field, E_g first decreases to zero at a critical field strength of ±0.142 V/Å and then reopens on further increase in the magnitude of the field. This phenomenon offers the possibility to control on/off and charge/spin conductance of helical edge states by the external field in QSH-based devices [21c-g].

Another allotrope of MoS_2 (1S-MoS2) possesses square-octagon ring structure with *D4h* symmetry [22a-d] which can be viewed as a three-layer stacking of Mo and S atoms, wherein Mo atoms are sandwiched between layers of S atoms [Fig. 17(a)]. The equilibrium lattice constants are calculated to be 6.336 Å [22c]. The inversion symmetry also exists in 1S structure. Note that four- and eight-membered rings structures found at grain boundaries of 1H-MoS_2 [22e]. The calculated phonon dispersion of 1S-MoS_2 possesses positive frequencies of all phonon branches in the whole Brillouin zone indicating the dynamic stability of 1S-phase of MoS_2 [Fig. 17(b) & (c)]. Electronic band structure of 1S-MoS_2 without considering SOC, shows valance band maximum (VBM) and conduction band minimum (CBM) touching at the same point indicating it as gapless semiconductors [22e]. VBM and CBM are mainly contributed by the $d_{x2\text{-}y2}$ and d_{z2} orbitals of the Mo atoms, respectively [Fig. 17(d)]. Besides, this the CBM + 1 at the 'Γ' point is mainly contributed by $d_{x2\text{-}y2}$ orbitals. Electronic band dispersion of 1S-MoS_2 in two-dimensional *k* space around the touching point at Fermi level confirms the touching of VBM and CBM at same point [Fig. 17(e)]. By turning SOC on, imposes a band exchange between CBM and CBM +1 at the 'Γ' point that results into a SOC-induced direct band gap of 24 meV in 1S-MoS_2 [Fig. 17(d) & (e)].

The topological Z_2 invariant is calculated to be Z_2 = 1 indicating 1S-MoS_2 monolayer as nontrivial 2D TIs. Considering the sizable nontrivial band gaps, the QSH effect can be readily realized at room temperature. By carefully examining the parities of the low-energy bands, it is found that no parity exchange between the valence and conduction bands occur [22c]. Therefore, SOC does not induce any band inversion between the valence and conduction bands at the TRIM. The only effect of SOC is to break the degeneracy at the touching point and to open an insulating gap. This is different from some well-known TIs, such as Bi_2Se_3 [23a], where the SOC is responsible for the band inversion. Such characteristics of 'intrinsic nontrivial band order' have also been found in several other systems, such as the chemically modified Bi and Sn honeycomb lattices [23b,c]. Also, a porous allotrope of monolayer MoS_2 (g-MoS_2) consisting of the square-hexagonal structure has been predicted to be QSH insulator [23d] and the calculated nontrivial gap as large as 109 meV is higher than 1T'-MoS_2 and 1S-MoS_2. In contrast to 1T'- and 1S-phase of MoS_2, the QSH effect in g-MoS_2 originates from the pure d-d band inversion. Such new polymorph dramatically enriches the QSH insulator family based on MoS_2.

4. Growth methods

4.1. Mechanical exfoliation

Mechanical exfoliation (ME) is simply "peeling" or "cleaving" the bulk crystals with the help of an adhesive tape or 'rubbing' bulk crystals against a solid surface, is categorized as a top-down technique, has been widely used for the fabrication of single- and/or few-layer systems from their bulk counterpart [1d,11b]. As discussed, the atoms in 2D TMDCs are covalently connected to their neighboring layers, via van der Waals bonding along the third axis. The weak interlayer van der Waals forces enable the facile exfoliation of the TMDCs. ME has been successfully applied for the fabrication of few layers of MoS_2 (thickness ~3–10 nm) [10d-g]. The Scotch tape, chemical and mechanical exfoliation methodologies are the most common techniques to produce and disperse TMDC layers in polar solvents. This technique produces a very clean, high quality samples [10h,i]. Optical and AFM images of single layer MoS_2 is shown in Fig. 18 and Fig. 19 respectively [4e,14c]. However, large scale production is not possible adopting this methodology, so limited to prepare samples for research purpose only.

4.2. Chemical vapor deposition

Chemical vapor deposition (CVD) is another common and extensively used techniques to synthesize and understand the

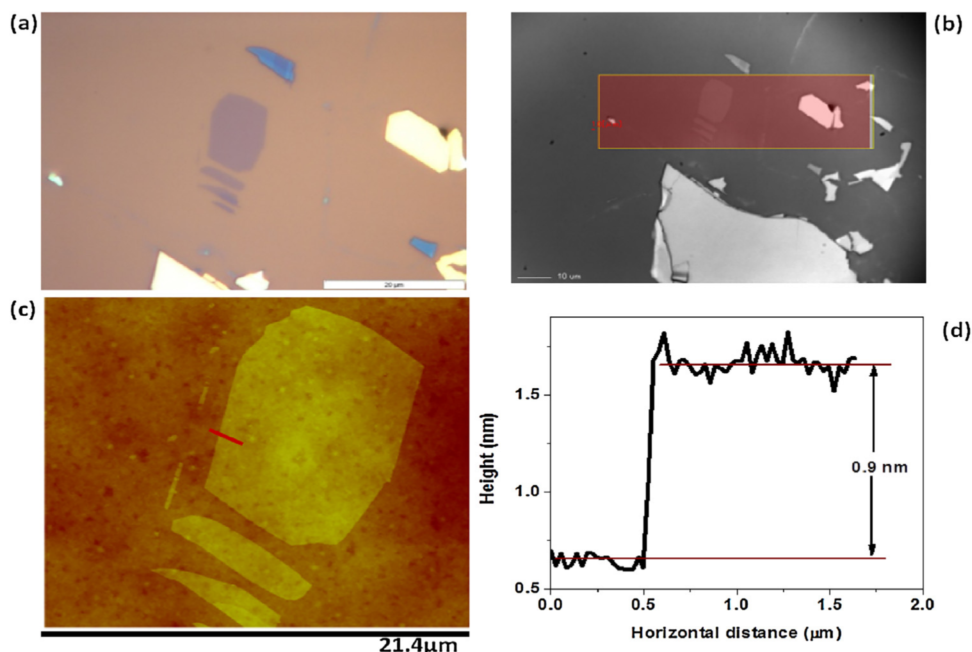

Fig. 18. Single-layer of MoS_2 sheet on 300 nm SiO_2/Si substrate obtained using micromechanical cleavage method. (a) An optical image, (b) Raman image, (c) AFM image, and (d) corresponding AFM height profile respectively. (*Reproduced with permission from ref. 4(e) ACS Nano, 4879, 2013.*)

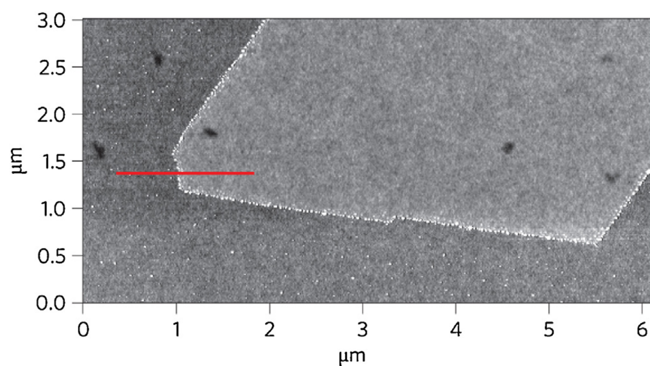

Fig. 19. Atomic force microscope image of the single layer of MoS_2 on a silicon substrate. (*Reproduced with permission from ref. 14(c). Nature Nanotechnology, 2011, 6, 147–150.*)

microscopic growth mechanism of 2D TMDCs. Traditionally, the sulphurization of the MoO_3 (Molybdenum (VI) oxide) powder to grow monolayer MoS_2 has been accepted and widely studied [24,25a–c]. Benefited from the moderate melting and evaporation temperatures, Li et al. successfully demonstrated that at favorable growth conditions, the MoO_3 powder is a suitable precursor for MoS_2 thin films growth using CVD technique [24,25a-c] (Fig. 20) [25c]. In another experiment, Li et al. describe growth mechanism of CVD grown MoS_2 layers, assisted by seeding the substrate with graphene-like species but the study lacks whole grains and grain boundary characterization [25d]. Later on, Li et al. concluded that the pretreatment of substrates with various aromatic molecules including reduced graphene oxide, perylene-3,4,9,10-tetracarboxylic acid tetra-potassium salt (TPAS) and perylene-3,4,9,10-tetracarboxylic dianhydride (PTCDA) before deposition helps in subsequent MoS_2 growth [16c]. The reaction mechanism for the growth of MoS_2 layer was proposed to be:

$$MoO_3 + x/2S \rightarrow MoO_3 - x + x/2SO_2 \text{ and}$$

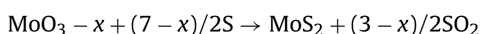

$$MoO_3 - x + (7 - x)/2S \rightarrow MoS_2 + (3 - x)/2SO_2$$

where $x = 1$ once an intermediate phase formed. However, a systematic study describing detail on growth parameters are still missing this, and the fabrication of large area MoS_2 is still challenging [25c]. Recently, Henz's and Ajayan's group separately reported CVD-based procedure to fabricate large-area, highly crystalline MoS_2 layers by sulphurizing vapor-phase MoO_3. These experiments show the crucial role of MoO_3 during the growth of MoS_2 which was controlled by the diffusion of vapor-phase MoO_3. Several growth stages from random nucleation to small triangular domains and their evolution to the continuous film were systematically studied. The method is very efficient and promises large-area continuous films of single-layered MoS_2. Their findings were in contrast to graphene growth on Cu foil by CVD method, and with complicated nucleation process on bare SiO_2 substrates [25d,e]. These observations strengthen the argument made by Li at al. on CVD-grown MoS_2 and interpreting the importance of control nucleation which is essential for the growth of large-area MoS_2 monolayers [25c]. The fundamental requirements of this approach on the edge-based nucleation growth bear a resemblance to the observations and theoretical predictions for the growth of some other layered materials [25d,e].

4.2.1. *Vapor phase growth*

For the fabrications of large-area MoS_2 thin films, vapor phase deposition stands as an appealing and versatile strategy. Sulphurization of solid MoO_3 films have involved many researchers and exposed a straightforward technique for the synthesis MoS_2 [26a,b]. However, the quality and the small grain size (~20 nm) of thus grown samples is not admirable and possess low carrier mobility (0.004–0.04 $cm^{-2}V^{-1}s^{-1}$) in comparison to mechanically-exfoliated samples (01–10 cm^{-2} V^{-1} s^{-1}) [26b]. In order to fabricate high-quality, uniform and large-area TMDCs with good electrical performance, efforts have been devoted to the thermolysis the precursor containing Mo and S atoms. Li et al. [26b] reported a two-step thermolysis process of ammonium thiomolybdate resulting large-area, highly crystalline MoS_2 thin films on divers insulating substrates (Fig. 21). During the thermolysis the ammonium thiomolybdate precursor dissociated into MoS_2, NH_3 and S

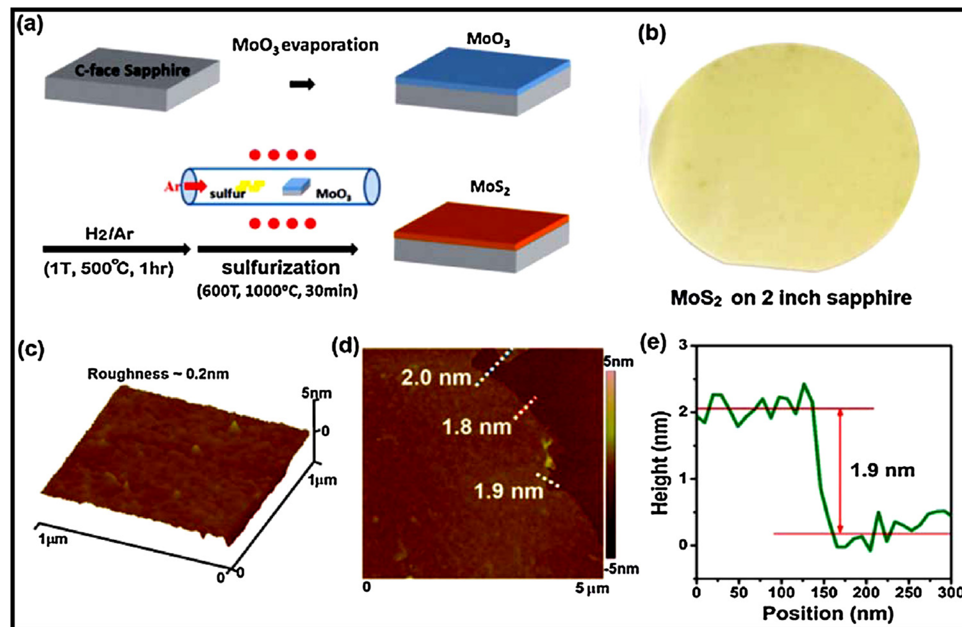

Fig. 20. (a) Schematic illustration of the MoS_2 layers by MoO_3 sulfurization. A layer of MoO_3 (3.6 nm) was thermally evaporated on the sapphire substrate. The MoO_3 was then converted to a MoS_2 by a two-step thermal process. (b) MoS_2 layer is grown on a sapphire wafer. (c and d) Surface topographic images obtained by AFM. (e) A selected cross-sectional height profile is showing the thickness of the MoS_2 layer. (*Reproduced with permission from ref. 25(b). Nanoscale, 2012, 4, 6637.*)

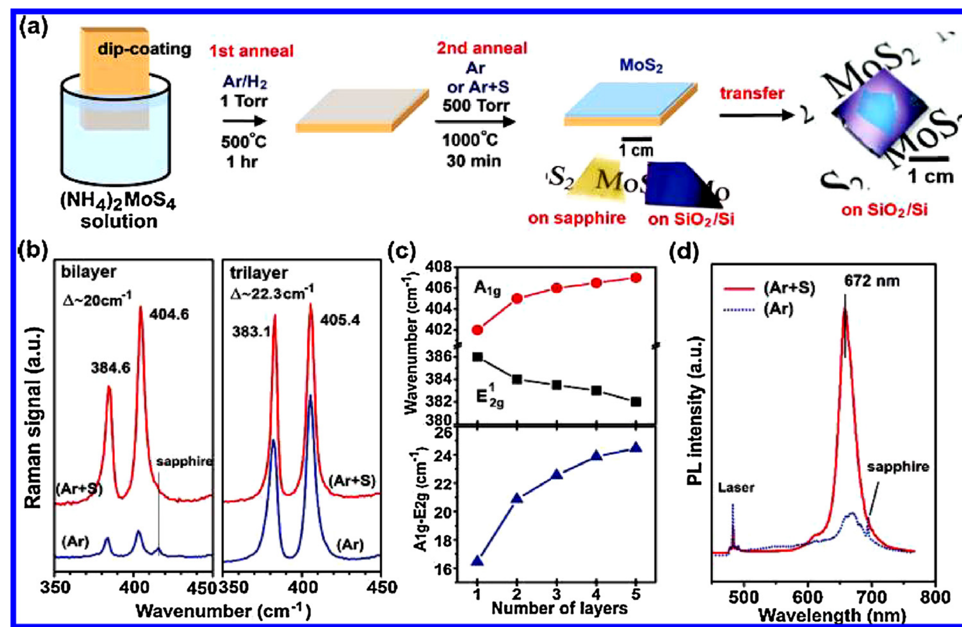

Fig. 21. (a) Schematic illustration for the Synthesis of MoS_2 thin layers on insulating substrates by two-step thermolysis process. (b) Raman spectra for the bi and tri-layer MoS_2 grown on sapphire substrates. (c) Energies of the two characteristic Raman peaks for the micromechanically exfoliated MoS_2 films with different layers. (d) The PL intensity of the tri-layer MoS_2 thin films prepared in (Ar+S) is stronger than those developed in pure Ar. (*Reproduced with permission from ref. 26(b), Nano Letters 78 (3), 1538–1544 (2012).*)

at/above 800 °C [26b]. The multistep transformation reaction from $(NH_4)_2MoS_4$ into MoS_2 involves fairly complex chemistry. The transistor devices fabricated with MoS_2 thin layers using a bottom gate geometry exhibit n-type behavior with a significantly improved on/off current ratio [26b].

4.3. Liquid-phase preparations

The bulk TMDC crystals exfoliated into mono- or few-layer nanosheets found to meet their full range of potentials. However, the yield of exfoliated TMDCs materials (i.e., single, bi- and multilayer) produced by mechanical exfoliation, are unambiguously less which is disadvantageous for their commercial utilization. To obtain large quantities of mono- or few-layer TMDCs nanosheets, a solution processing strategy is strongly required. Recently, Coleman et al. proposed liquid-phase exfoliation of bulk MoS_2 powders in an organic solvent with the help of ultra-sonication and demonstrated the simple fabrication of the exfoliated material [18f]. N-methylpyrrolidone (NMP) is used as most popular solvent, which is universal to exfoliation of most TMDCs [18f]. This method gives thin sheets of MoS_2 with thicknesses around 4–10 nm, corresponding to 6–18 layers. However,

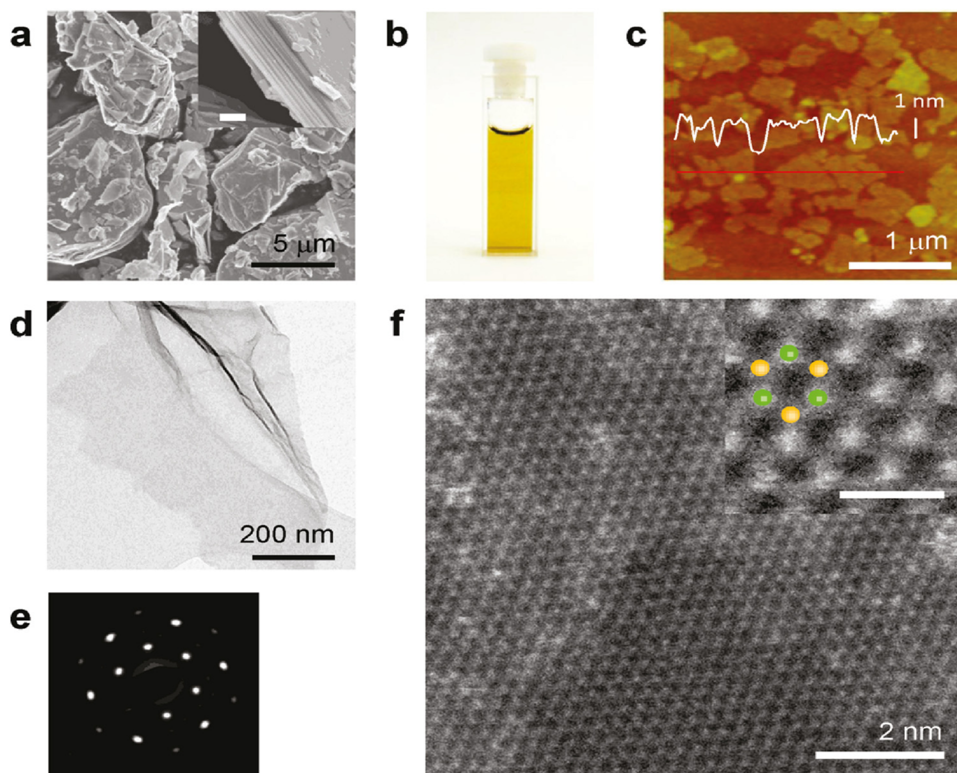

Fig. 22. (a) SEM images of MoS_2 powder. The Inset shows higher magnification image of the layered structure. The scale bar is 400 nm. (b) Photograph of a standard chemically exfoliated MoS_2 suspension in water. (c) AFM image of individual exfoliated MoS_2 sheets after annealing at 300 °C. Height profile along the red line is overlaid on the picture. (d) TEM image of an as-deposited MoS_2 sheet on a holey carbon grid. (e) SAED pattern from the MoS_2 layer in (d) showing the hexagonal symmetry of the MoS_2 structure. (f) HAADF STEM image of monolayer MoS_2 annealed at 300 °C in Ar. Inset is a blow-up image showing only Mo (green dot) and S (orange dot) atoms and their honeycomb arrangement. The scale bar is 0.5 nm. The white blur on the surface of the sheet is possibly due to carbon residues from the intercalation and exfoliation processes. (*Reproduced with permission from ref. 28(a) Nano Lett. 2011, 11, 5111–5116.*)

monolayers were difficult to produce by this technique. After the success of Colemen's pioneer work, LPE was also successfully applied to synthesize 2D material phosphorene using benzonitrile as liquid media under inert atmosphere [26c,f]. On the other hand, Morrison and co-workers reported that Li-intercalated MoS_2 could be exfoliated into monolayers via forced hydration, yielding a stable colloidal suspension [26d]. This method provides a flexible way toward the assembly of MoS_2 sheets into thin films [27a-c] that can be utilized for photovoltaic applications [27d]. Though, exfoliation of MoS_2 by Li-intercalation changes the fundamental properties of MoS_2 [27e]. However, the disadvantage of this method is it requires a long time (days) yielding smaller size 2D nanosheets. Fig. 22 shows detailed characterizations of the MoS_2 layers obtained by liquid-phase exfoliation of bulk MoS_2 powders in an organic solvent [28a]. This method is not suitable for the production of high quality materials for their potential application in optical, electrical, and electrochemical measurements. However, the products obtained from this method can be used for catalysis, supercapacitors and sensors etc. where the compromised material quality is not an issue [27f-g]. Laser ablation of bulk crystals is an example of a less common top-down method [10i].

4.4. MoS_2 film fabricated by RF sputtering

Recently, Hussain et al. reported a simple and scalable approach for the synthesis of bi- and few layers MoS_2 films via RF sputtering followed by the post-deposition annealing method. In their experiment, MoS_2 films were fabricated using a MoS_2 target in the sputtering system. To improve the crystalline quality of as-sputtered samples, thin films were subjected to post-deposition annealing at 700 °C in Sulfur and Argon environment [28b]. The investigation confirmed the growth of continuous MoS_2 film. The process can be easily controlled by controlling the reaction parameter to grow bilayer as well as few layers MoS_2 films (Fig. 23). The Raman and photoluminescence (PL) spectra confirmed the crystalline quality of the MoS_2 films. The mobility was evaluated to be $\sim$29 $cm^2\,V^{-1}s^{-1}$ with the current on/off ratio $\sim$104 for bilayer and $\sim$173–181 $cm^2\,V^{-1}\,s^{-1}$ for the few-layer MoS_2 system. Hussain et al. concluded that the higher mobility behavior in their study could be attributed to low charged impurities of the film along with the dielectric screening effect by an interfacial MoO_xSi_y layer. The authors further argued that RF sputtering followed by post-deposition annealing opens up the new possibilities of mass production of large area MoS_2 films [28b].

In a similar experiment, Hussain et al. discussed the efficient layer-controlled, continuous and large-area MoS_2 growth onto SiO_2/Si substrate by RF sputtering followed sulfurization adopting some modification to their earlier experiments [28c]. As compared to their previous study, the number of MoS_2 layers here can easily be controlled by adjusting initial sputtering time. The MoS_2 transistors fabricated on thus grown MoS_2 films exhibited high mobility values $\sim$21 $cm^2V^{-1}s^{-1}$ (bilayer) and $\sim$25 $cm^2V^{-1}s^{-1}$ (trilayer), with significantly high on/off ratios in the range of $\sim$107 (bilayer) and 104–105 (trilayer), respectively [28c].

4.5. Atomic layer deposition (ALD)

Atomic layer deposition (ALD) is a thin film deposition method based on self-limiting mechanism. ALD can control film thickness at an atomic scale precision while forming highly uniform and conformal thin films on the large-area. Recent advances in the synthesis of 2D TMDCs have shown that atomic layer deposition

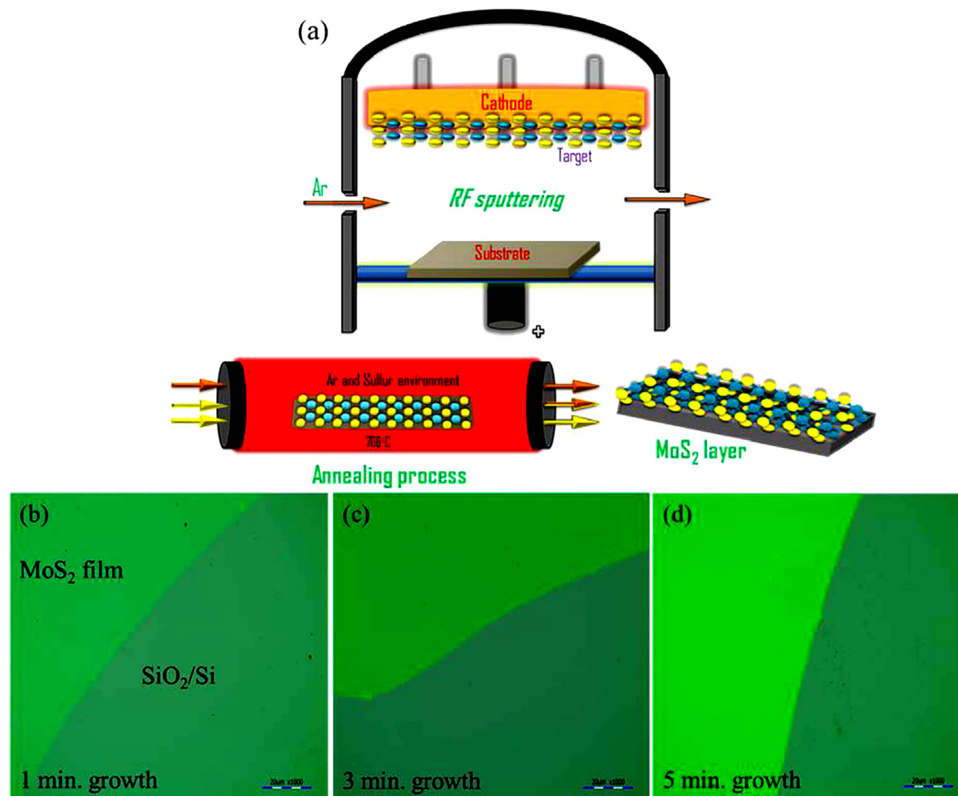

Fig. 23. (a) Schematic illustration of the RF sputtering technique to prepare MoS_2 thin films. Annealing at elaborated temperature was performed to enhance the crystalline quality of sputter grown MoS_2 films under Ar/S environment. (b-d) represents optical images of MoS_2 films grown on SiO_2/Si substrate for (b) 1 min; (c) 3 min, and (d) 5 mins sputtering. (*Reproduced with permission from ref. 28(b) Scientific Reports, 2016, 6, 30791.*)

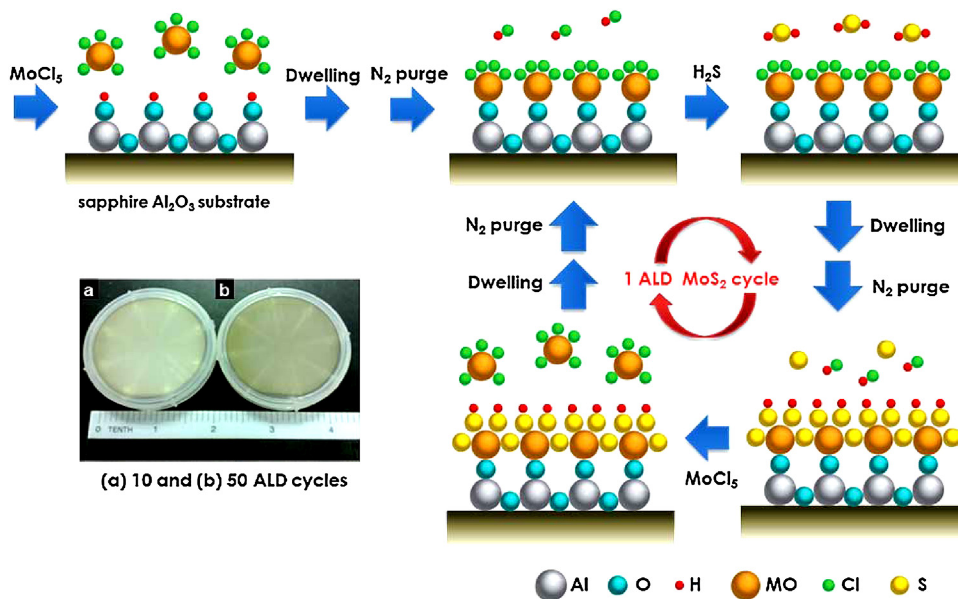

Fig. 24. Schematic illustrations of the MoS_2 film fabricated by atomic layer deposition method. The optical images show (a) 10 and (b) 50 cycles of the ALD MoS_2 film grown on a 2-inch sapphire (001) substrate. (*Reproduced with permission from ref. 28(d) Nanoscale, 2014, 6, 10584.*)

(ALD) of the metal oxide and subsequent sulfurization could offer a method to synthesize large-area MoS_2 with excellent layer control over the entire substrate. In the recent efforts by Loh et al. reported on the growth of controlled single to multilayer MoS_2 film by using the ALD technique at 300 °C on a sapphire wafer [28d]. In their process, ALD provides precise control over MoS_2 film thickness due to the pulsed introduction of the reactants and self-limiting reactions of $MoCl_5$ and H_2S precursors as shown in Fig. 24. Due to the self-limiting reactions of the vapors, the number of layers can be precisely controlled by adjusting the number of deposition cycles. Post-deposition annealing was introduced to improve the crystallinity as shown in Fig. 25, which was evident from the presence of triangle-shaped crystals exhibiting the strong photoluminescence in the visible range [28d]. However, ALD has some

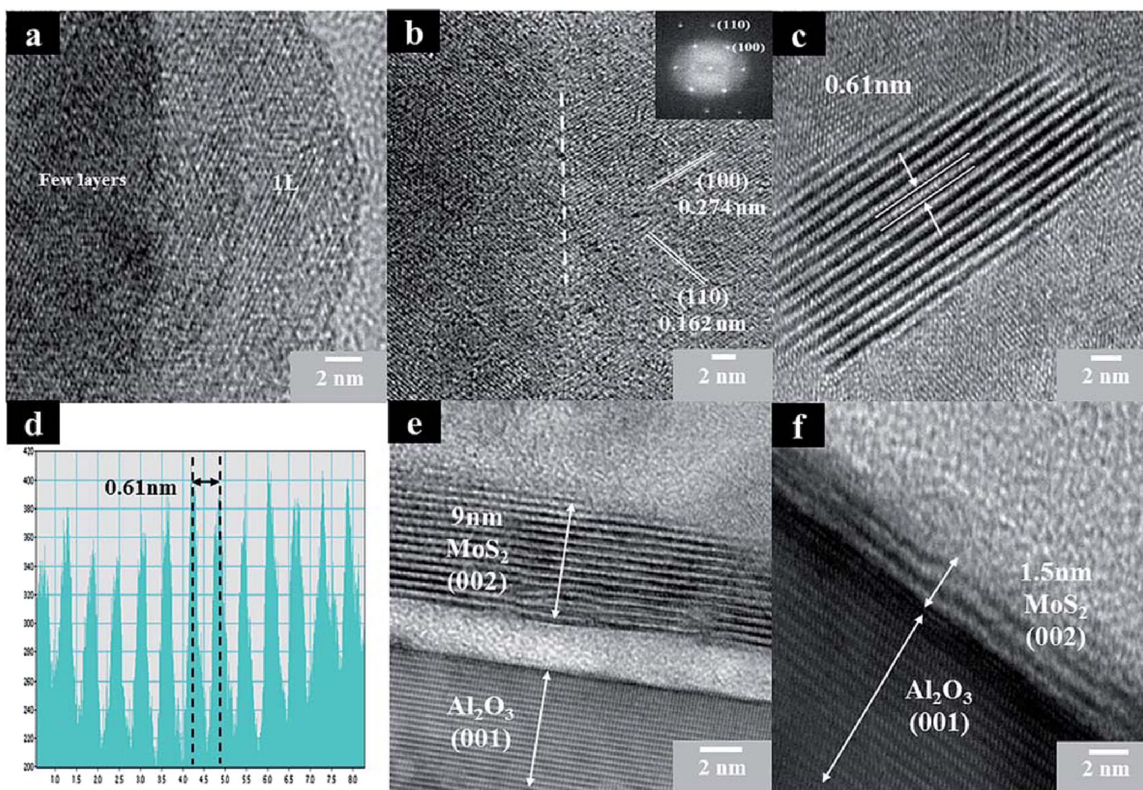

Fig. 25. (a) TEM image of single and few-layer MoS_2 film grown on sapphire (001) substrate by ALD technique. (b) The TEM image of the MoS_2 film revealing high crystallinity of the film produced by ALD with the hexagonal lattice structure (inset image). (c) Lattice spacing (d) The line profile depicting the spacing between layer (c). Cross-sectional TEM view of (e) 50 cycles and (f) 10 cycles ALD MoS_2 film on the sapphire substrate. (*Reproduced with permission from ref. 28(d). Nanoscale, 2014, 6, 10584.*)

inherent challenges like growing large area oxide films with sub 1 nm nucleation, and the necessary steps are still to be unexplored.

A very recent study on the synthesis of the MoS_2 film, Grossman et al. [28e] reported, control atomic layer deposition of molybdenum oxide nucleation followed by sulfurization to produces large-area MoS_2 monolayers. In their work, Grossman et al. demonstrated that the necessary process required achieving sub 1 nm nucleation domains formed by oxide deposition. Subsequently, fabrication of the MoS_2 films was performed by the sulfurization of oxides deposited. Large-area, uniform MoS_2 films were achieved by optimizing the effects and surface treatments on the ALD nucleated Mo oxide and the post sulfurization process [28e].

For better understandings of the controlled oxide deposition, film chemistry analysis during sulfurization, various temperature profiles revealing sulfur incorporation and molybdenum reduction were studied. Tunable film thickness with centimeter-scale monolayer growth was successfully achieved (Fig. 26) [28e]. In this study, a higher temperature was required for the formations of 2-H MoS_2 crystal structure.

5. Applications

5.1. TMDCs transistors

TMDCs have unique features like stability in air, the absence of a short-channel effect, no dangling bonds, and high mobility comparable to the Si which makes them attractive as an ideal channel material for FETs [12a,24,25]. The earliest application of TMDCs for FETs was reported in 2004, where WSe_2 crystals showed mobility comparable to the best single-crystal Si FETs (up to 500 cm^2V^{-1} s^{-1} for p-type conductivity at room temperature), ambipolar behavior with a 10^4 on/off ratio at a temperature around 60 K [29a]. Kis and co-workers for the first time reported a top-gate transistor based on monolayer MoS_2. The device showed excellent on/off current ratio ($\sim 10^8$), n-type conduction, the room-temperature mobility of >200 $cm^2\,V^{-1}\,s^{-1}$ and a subthreshold swing of 74 mV per decade [14d]. The cross-sectional view of MoS_2 transistors and its performance is shown in Fig. 27. Later-on Walia et al. also fabricated transistors based on MoS_2 with aluminum, tungsten, gold, and platinum contacts [29b]. From their work, it was evident that lower work functions of the contact metals lead to a smaller Schottky barrier size and thus higher charge carrier injection through the contacts. The study indicates that choosing a suitable metal contact is crucial in tuning the barrier height at the interface of the metal semiconductor. In another study, Kang et al. presented high-performance MoS_2 transistors with low-resistance Mo contacts [29c]. Density functional theory (DFT) simulations indicate Mo can form a high-quality contact interface with monolayer MoS_2 with zero tunnel barriers and zero Schottky barriers.

Recently, graphene has been used as an electrode for MoS_2 transistor because it forms a subtle Schottky barrier. Graphene is well known to possess high electrical conductivity, optical transparency, and flexibility, a flexible and transparent MoS_2 transistor has also been fabricated using graphene as source-drain electrodes [29d]. Lee et al. have compared graphene vs. metals source/drain contact for MoS_2 transistors and found that the mobility is higher for graphene contacted MoS_2 as compare to metal contacted [29e-f]. In another study, Roy et al. found that 2D materials for all components, including MoS_2 as the channel material, hexagonal BN as top gated dielectric and graphene as electrodes works well [30b]. In a similar study, Singh et al. demonstrated low-voltage, high-performance field-effect transistors fabricated using single-layer graphene with multilayered MoS_2 as a channel (Fig. 28) [30c]. The two terminal mobility of graphene contacted to monolayer MoS_2

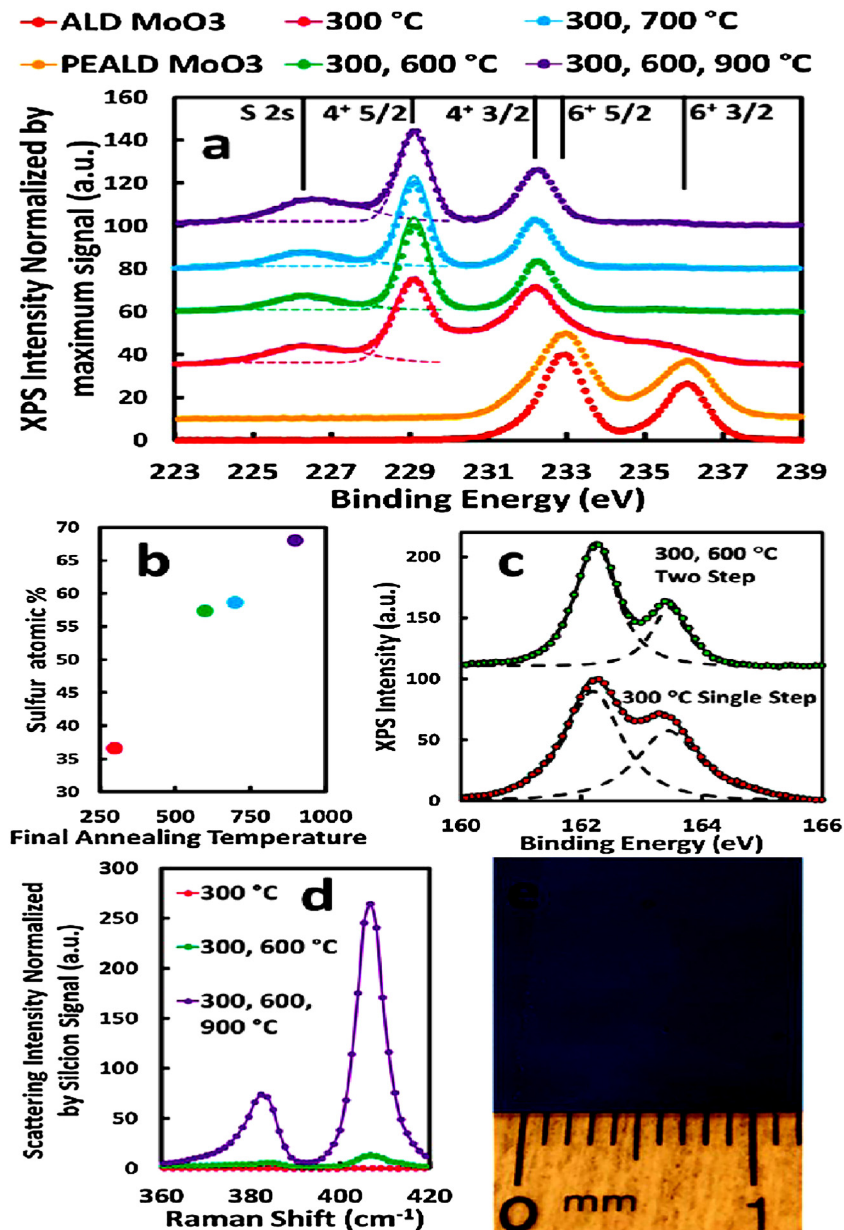

Fig. 26. Multistep sulfurization of (a) Mo 3d XPS normalized by the maximum signal for as-deposited ALD and PEALD films following single step processing at 300 °C, 2 step processing first at 300 °C and then at 600/700 °C, and 3 step processing at 300, 600, then 900 °C. Dashed lines represent fitted contributions of S 2s and Mo^{4+} $3d_{5/2}$, and the solid line represents total contribution. (b) The Atomic percentage of sulfur based on the Mo 3d and S 2s peaks showing partial incorporation of sulfur during a 300 °C single step anneal and final stoichiometric incorporation via a three-step anneal. (c) S 2p XPS spectra with broad peaks at 300 °C indicating disorder and poor uniformity in a chemical environment. By 600 °C in a two-step anneal, peaks are sharp (binding energies of 162.2 eV for S 2p3/2 and 163.5 for eV 2p1/2 respectively). Dashed lines indicate fits for the 2p3/2 and 2p1/2. Solid lines represent the sum of the fits. As the sulfur content increases at higher temperature, Raman spectra (d) show the emergence of the A_{1g} and E_{2g} peaks characteristic of the 2H structure of multilayer MoS_2. (e) Optical image of 4.5 nm thick MoS_2 following transfer to a larger 300 nm SiO_2 on Si substrate showing centimeter scale uniformity achieved with ALD and the post sulfurization process. (*Reproduced with permission from ref. 28(e). Chem. Mater., 2017, 29, 2024–2032.*)

at room temperature using 15 nm Al_2O_3 as the top-gate dielectric layer was found to be 131.2 $cm^2 V^{-1} s^{-1}$. The reported values are higher than the previously reported metal/graphene-contacted MoS_2 [30c]. Furthermore, Singh et al. tuned the threshold voltage, charge carrier concentration and mobility of the single, bi-and multilayer transistors of MoS_2 with the combination of gases under ultraviolet light exposure [30d] and by implementing gold (Au) metal adsorbate [30c].

5.2. Field emission

Field emission studies of layered MoS_2 sheets at the base pressure of $\sim 1 \times 10^{-8}$ mbar were investigated. A turn-on field to draw 10 $\mu A/cm^2$ field emission current density for MoS_2 layers was reported to be 3.5 V/μm (Fig. 29). The turn on values found to be notably lower than graphene. The emission current-time plots show excellent stability over the period of 3 h. Due to the weak turn-on field and planar (sheet-like) structure, MoS_2 may have potential application in futuristic vacuum microelectronics and flat panel display [7d].

5.3. Photovoltaics and photodetection

Photovoltaics and photodetection are another interesting filed where TMDCs thin films can be employed. A Schottky-barrier solar cell fabricated using few-layer, CVD-grown MoS_2 film serving as

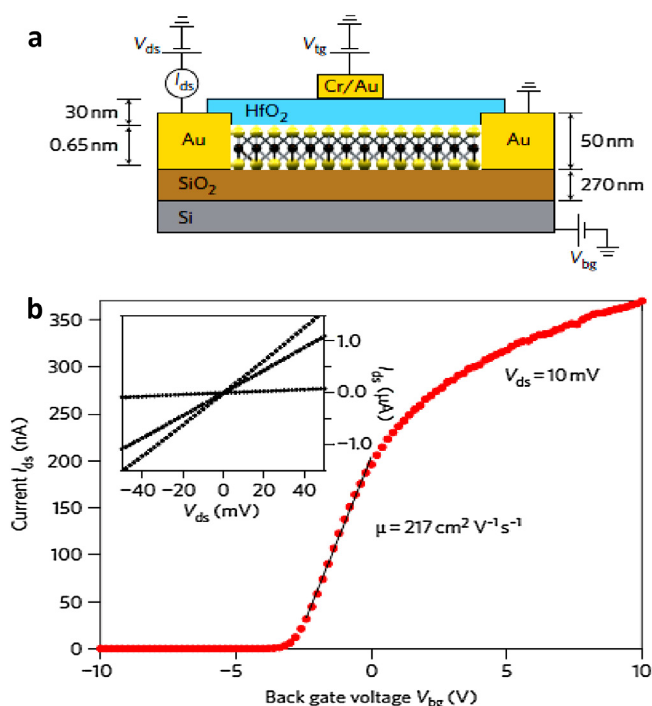

Fig. 27. (a) A cross-sectional view of the structure of a monolayer MoS_2 FET. (b) Transfer characteristic at room temperature for the FET with 10 mV applied bias voltage Vds. Backgate voltage Vbg is being implemented to the substrate, and the top gate is disconnected. The inset shows the I_{ds}–V_{ds} curve acquired for Vbg values of 0, 1 and 5 V. (*Reproduced with permission from ref. 14(d). Nature Nanotechnology, 2011, 6, 147–150.*)

the critical photo-active layer is recently reported [30f]. Fig. 30 shows CVD growth setups to synthesize MoS_2 on SiO_2/Si substrates. Fig. 30(b–e) realizes the steps for transferring MoS_2 films on the desired substrates [30f]. Fig. 31 provides information on the (a) Schematic cross-sectional view of the Schottky barrier solar cell on an ITO substrate with Au contact. (b) Energy band diagram of the solar cell with the formation of a Schottky-barrier between the MoS_2 nanomembrane with Au metal contact.

The performance of solar cell depending on MoS_2 thickness was investigated and presented in Fig. 31. Fig. 32(a) and (b) shows dark and illuminated *J*–*V* characteristics of the as-fabricated Schottky-barrier solar cells with MoS_2 thicknesses of 110 nm and 220 nm, respectively. The output power as a function of voltage in a solar cell is shown in the insets of Fig. 32(a) and (b), respectively [30f]. The study concluded that higher the MoS_2 thickness resulting higher the JSC values for a solar cell that is due to efficient photo-absorption in the thicker MoS_2 system which leads to a noteworthy alteration in the overall device performance.

The reported results on solar cell performance would promote continued efforts toward developing highly efficient Schottky-barrier solar cells captivating advantage of the unique interfacial properties of layered semiconductor nanostructures [30f].

5.4. Gas sensing

Recently, *Dravid's group* reported on the synthesis of large-area mono- to hex-layers MoS_2 sheets and identified using an optical microscope with the help of distinctly visible color contrast and further confirmed by AFM and Raman spectroscopy [4e]. The various MoS_2 sheets in the form of transistors were assessed for gas sensing performance with exposure to NO_2, NH_3, and humidity, at room temperature [4e]. Upon exposure of NO_2 and NH_3 gases, the MoS_2 transistors showed a decrease and increased in conductance, respectively with a substantial shift in the threshold gate voltage. Single-layer MoS_2 shows quick response but the low signal to noise ratio. The bi-to hex-layer MoS_2 shows sound sensitivity as well as proper intervention and recovery. These results indicate that 2- to 6-layer MoS_2 transistor-based devices exhibit excellent sensing performance at room temperature, compared to the existing solid-state sensors, with better sensitivity, quick response, and ability to sense lower concentrations. Fig. 33 shows the comparative study of sensing behavior with and without applying back gate voltage (+15 V) for 2-layer MoS_2 (a) NH_3, (b) NO_2 and 5-layer MoS_2 (c) NH_3 and (d) NO_2 [4e].

5.5. Hydrogen production

An ever increasing demand for energy in our society leads to the exploitation of non-renewable energy sources including fossil fuel paved the way for several environmental crises [31a]. As a consequence of the intensive use of fossil fuels, global warming is one of the principal threats due to the accumulation of greenhouse gases. Limited availability of rapidly exhausting fossil fuels has compelled researchers to accelerate the search for environment-friendly, renewable and sustainable alternative energy resources [31b-c]. To lessen the dependence on fossil fuels, hydrogen is considered as a promising cleaner-energy alternative in comparison to carbon-based fossil fuels as the combustion of hydrogen produces water

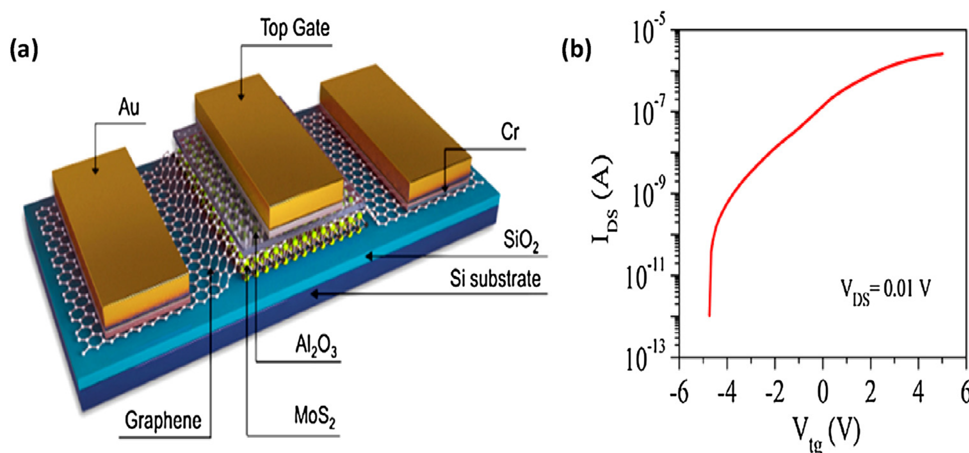

Fig. 28. (a) A cross-sectional view of the top-gated ML MoS_2, (b) Plot of I_{DS}-V_{tg} of the ML MoS_2 transistor at V_{DS} value of 0.01 V. (*Reproduced with permission from ref. 30(c). ACS Appl. Mater. Interfaces, 2016, 8, 34699–34705.*)

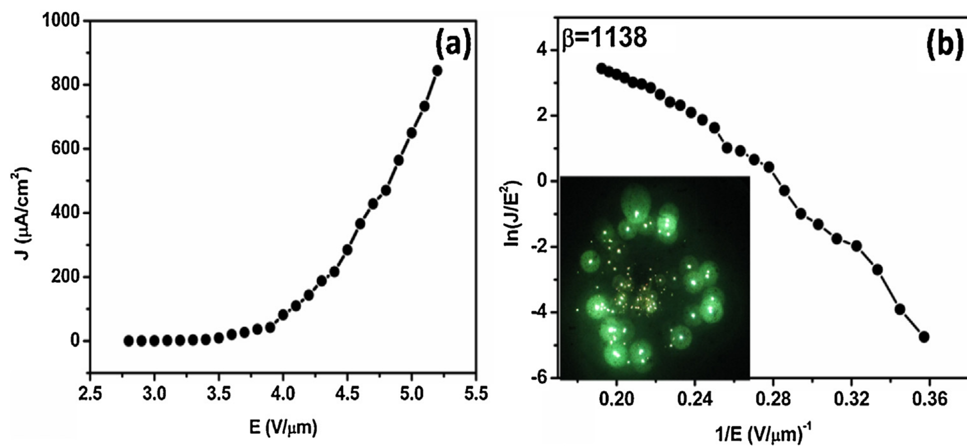

Fig. 29. Field emission characteristics of a multilayer MoS_2 system, (a) represent the applied electrical field behavior (J) as a function of current density (E). And (b) F-N plot showing non-linear behavior indicating emission current from the semiconducting emitter, the inset shows field emission pattern of a few layered MoS_2 recorded at a current density of 50 $\mu A/cm^2$. (*Reproduced with permission from ref. 7(d) Small, 2013, 9, 2730–2734.*)

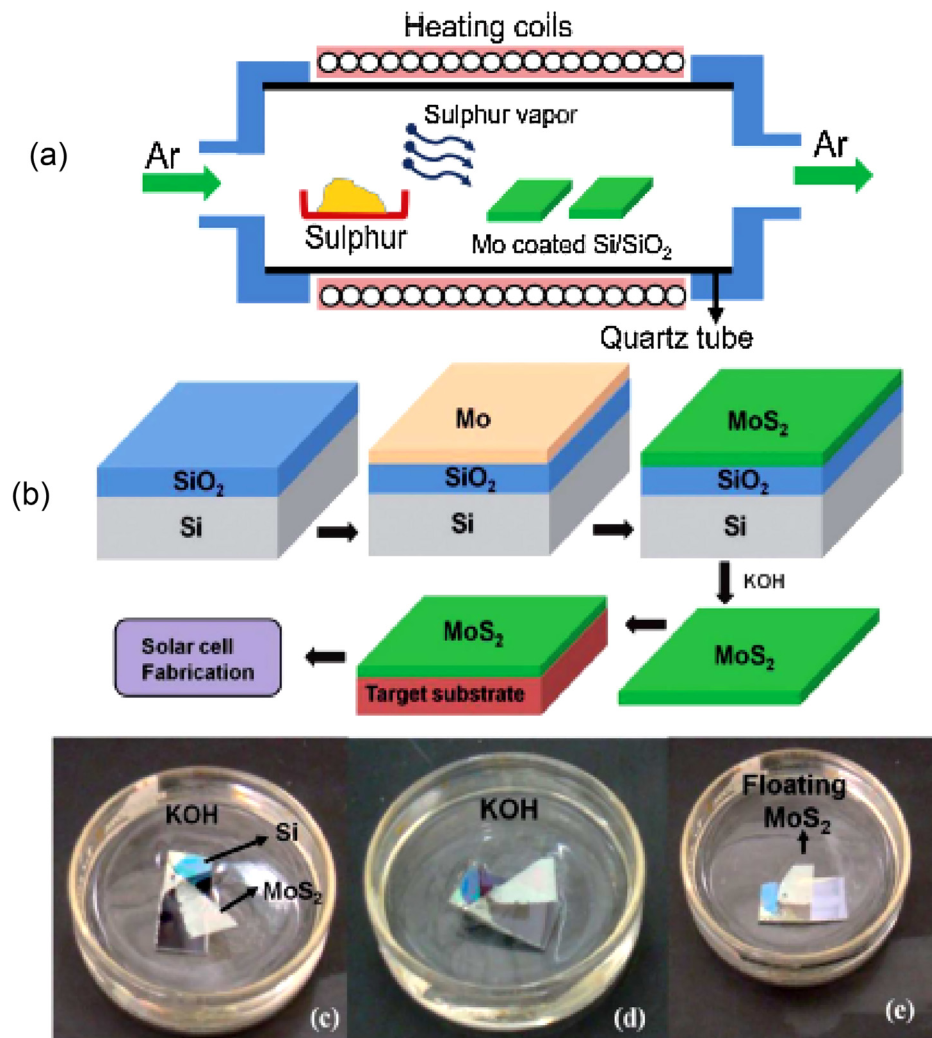

Fig. 30. (a) Schematic of the CVD growth setup of a MoS_2 nanomembrane on Si-SiO_2 substrate. (b) Major process steps involved in the synthesis of the MoS_2 nanomembrane, layer transfer, and subsequent fabrication of a Schottky-barrier solar cell. The KOH wet etching process was used to detach the MoS_2 nanomembrane from SiO_2–Si substrate. (c and d) Partially floating MoS_2 nanomembrane in KOH solution. (e) Free-floating MoS_2 nanomembrane in KOH to be transferred onto an ITO-coated glass substrate for solar cell fabrication. (*Reproduced with permission from ref. 30(f), Nanoscale 2012, 4, 7399–7405.*)

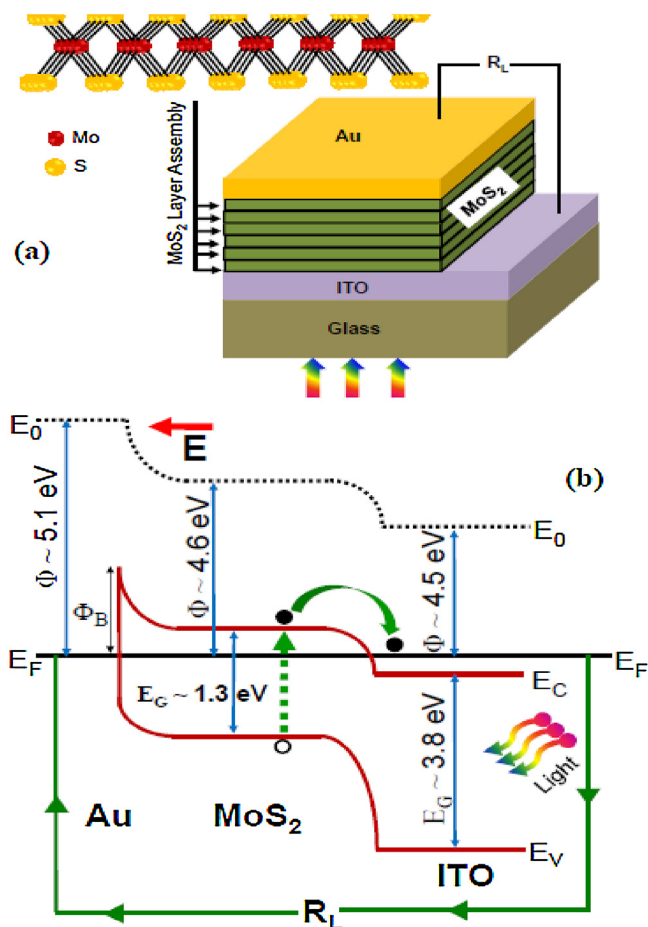

Fig. 31. (a) Schematic cross-sectional view of the demonstrated Schottky barrier solar cell structure showing a stack of MoS_2 nanomembrane on an ITO substrate with Au contact. (b) Energy band diagram of the solar cell with the formation of a Schottky-barrier between the MoS_2 nanomembrane and Au metal contact. (*Reproduced with permission from ref. 30(f) Nanoscale 2012, 4, 7399–7405*.)

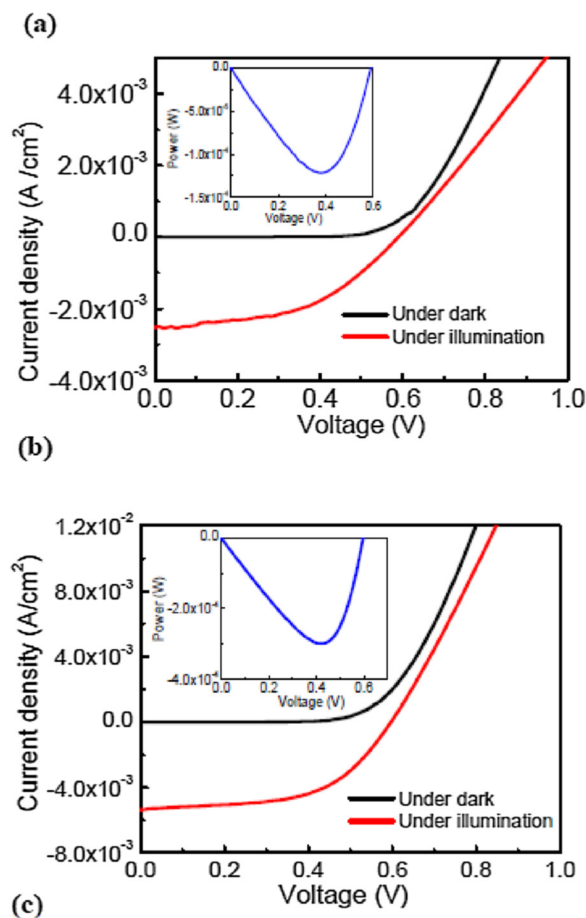

Fig. 32. Measured dark and illuminated J–V characteristics of the Schottky-barrier solar cells with a stack of MoS_2 nanomembrane having thicknesses of (a) 110 nm and (b) 220 nm. Inset of each figure shows the power output as a function of voltage for the fabricated solar cell. (*Reproduced with permission from ref. 30(f) Nanoscale 2012, 4, 7399–7405*.)

as the only by-product without emission of any toxic or greenhouse gases. Hydrogen production using environment-friendly photo/electro/chemical methods is critically important and significantly promising approach for the utilization of affordable, clean energy [31d-f]. Water splitting either by (1) electrocatalytic or (2) photo-electrocatalytic route requires the hydrogen evolution reaction (HER) to occur readily. Since the emergence of photocatalytic water splitting in 1972 [31g], HER received significant research attention. The production of hydrogen involves the utilization of precious noble metals (e.g., Pt, Rh, Pd, etc.) and their alloys [8i]. However, high cost and inadequacy, significantly hindering their industrial application. The scalable and sustainable hydrogen production demands efficient and robust earth-abundant electrocatalysts for the HER beyond precious-metal. Therefore, development of low-cost and earth-abundant catalysts as a competitive alternative to Pt-group metals is highly desirable.

6. Hydrogen evolution mechanism

The water-splitting reaction:

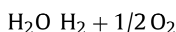
$H_2O\ H_2 + 1/2\,O_2$

Can be divided into two half-reactions: the water oxidation reaction (or oxygen evolution reaction [OER]) and the water reduction reaction (or HER). For this reaction to take place and to achieve the electrochemical water splitting, an energy $\Delta G = 237.1$ kJ/mol is required, which corresponds to a thermodynamic electrochemical potential of 1.23 V [8i]. Therefore, an external potential of ~1.23 V is sufficient (theoretically) for water splitting in an electrochemical cell assembly. However, the substantial kinetic barriers originating from the high activation energies required for the formation of reaction intermediates on the electrode surface which leads to overpotentials. Thus, for practical realization, a potential more than 1.23 V is needed for water splitting [8i].

The HER in an acidic environment typically involves three steps [32a]: (i) The first step is called the Volmer or discharge reaction with a Tafel slope of 120 mV dec^{-1} and can be presented as:

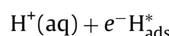
$H^+(aq) + e^- H^*_{ads}$

During this reaction between an electron and proton transfer, on the electrode surface generation and adsorbtion of hydrogen atom (H^*_{ads}) take place. The intermediate reaction could proceed two ways: either via the (ii) Tafel reaction or (iii) the Heyrovsky reaction.

In the Tafel reaction, two absorbed hydrogen atoms combine to generate H_2 gas with a Tafel slope of 30 mV dec^{-1}:

$2H^*_{ads}\ H_2(gas)$

Whereas Heyrovsky reaction takes place when another electron reacts with an adsorbed hydrogen atom and a proton from the solution to yield H_2 with a Tafel slope of about 40 mV dec^{-1} [32b,c].

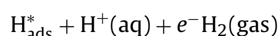
$H^*_{ads} + H^+(aq) + e^- H_2(gas)$

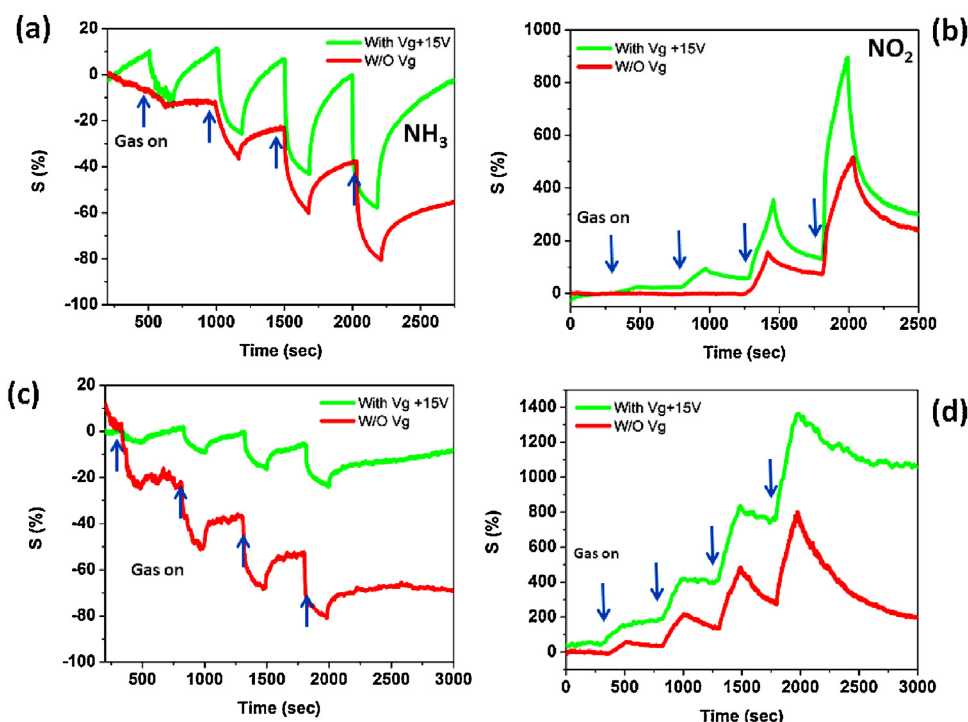

Fig. 33. Comparative sensing behaviors with and without applying back gate voltage (+15 V) for 2-layer MoS_2 (a) NH_3, (b) NO_2 and 5-layer MoS_2 (c) NH_3 and (d) NO_2. (*Reproduced with permission from ref. 4(e) ACS Nano, 2013, 7, 4879–4891.*)

It is quite evident from the reaction mechanisms that an adsorbed hydrogen (H^*_{ads}) as an intermediate is of vital importance. Since H^*_{ads} is always generated in the first Volmer reaction consecutively, takes part in each electrochemical reaction step in the course of HER. Furthermore, it has been well established that the H^*_{ads} energies for HER are moderated by optimum catalysts feature [32d]. The theoretical calculations providing insights for the catalytic activity with the help of density functional theory (DFT) while computing the Gibbs free energy for hydrogen adsorption ($\Delta G_H{}^*$) in the Volmer reaction has been proposed as an effective tool for HER catalytic activity [32e-g]. Pt-group metals with almost zero $\Delta G_H{}^*$ and the highest exchange current density are the best suitable materials for the HER, but due to several restrictions as mentioned above, their practical realization is hindered. Therefore, a non-Pt earth-abundant HER catalysts with nearly zero $\Delta G_H{}^*$ is highly desired. Significant research efforts have been devoted in the exploration of efficient, inexpensive, earth-abundant, and nontoxic catalysts for HER, e.g., metal alloys, chalcogenides, nitrides, phosphides, borides, carbides and their composites etc. [33,34]. Among several, two-dimensional (2D) layered transition-metal dichalcogenides (TMDCs) have received great attention because of their unusual physical/chemical properties originating from their unique crystal structures, with great promise for hydrogen production as HER catalysts [35a-c]. The last decade has witnessed the development of Molybdenum disulfide (MoS_2) conceivably the first earth abundant compound to be studied as a promising candidate of noble-metal-free HER catalyst [33d,f-i,35c-e]. MoS_2 with low cost, earth abundance, and excellent stability is suggested as a promising HER catalyst because of low $\Delta G_H{}^*$ close to that of noble metals [33f-i]. It is well documented that the bulk MoS_2 is not HER active catalyst [35f]. However; theoretical calculations predicted that the nanostructures of MoS_2 could serve as a promising HER catalyst [32f].

Recently, several crucial aspects have been developed to significantly enhance HER catalytic activity of nanostructured MoS_2 including (a) increasing active sites, (b) tuning the phase and electronic structure, (c) coupling with conductive scaffolds, (d) amorphous molybdenum sulfide, and (e) (amorphous) ternary compounds demonstrating meritoriously improved catalytic activity of MoS_2 [33f-i]. Inspired from the fact that the higher catalytic activity can be achieved along the edges of MoS_2, various nanostructures of MoS_2 including nanosheets, nanoflakes, nanowires, nanoparticles and mesoporous structures, have been fabricated to optimize the exposed active sites [33f-i]. It has been well established that the single-layered MoS_2 particularly with Mo-terminated edges, contribute predominantly to the HER catalytic activities [36a,b]. Theoretical calculations based on DFT simulation reveals that most of the HER activity is ascribed to the Mo-terminated edge MoS_2 owning lower hydrogen binding energy than the basal plane [32f,36c-f]. Some recent study based on DFT calculations claimed that the sulfur vacancy is the new catalytic site for HER in 2H-MoS_2 beyond the edges [36g].

Vertically aligned layers of MoS_2 and $MoSe_2$ thin films providing maximum exposure of the edges on the film surface have been reported by Kong et al. [37a] (Fig. 34(a-b)). In a different approach, MoS_2 nanoflowers grown on graphite substrates by chemical vapor deposition (CVD) method successfully exposed the abundant edges [37b]. Single-crystal MoS_2 nanobelts exhibiting high electrocatalytic hydrogen evolution efficiency have also been reported [37c]. Kibsgaard and co-worker adopted an elaborate strategy altering the MoS_2 surface to improve catalytic performance (Fig. 34(c-f)) [36c]. In another experiment, ultrathin MoS_2 nanosheets with a large number of defects were synthesized delivering improved catalytic performance [36d].

7. Composites with conductive hosts

A composite of MoS_2 with conductive frameworks is an effective method to improve the overall HER catalytic performance [33f-i]. Different conductive carbon nanostructures

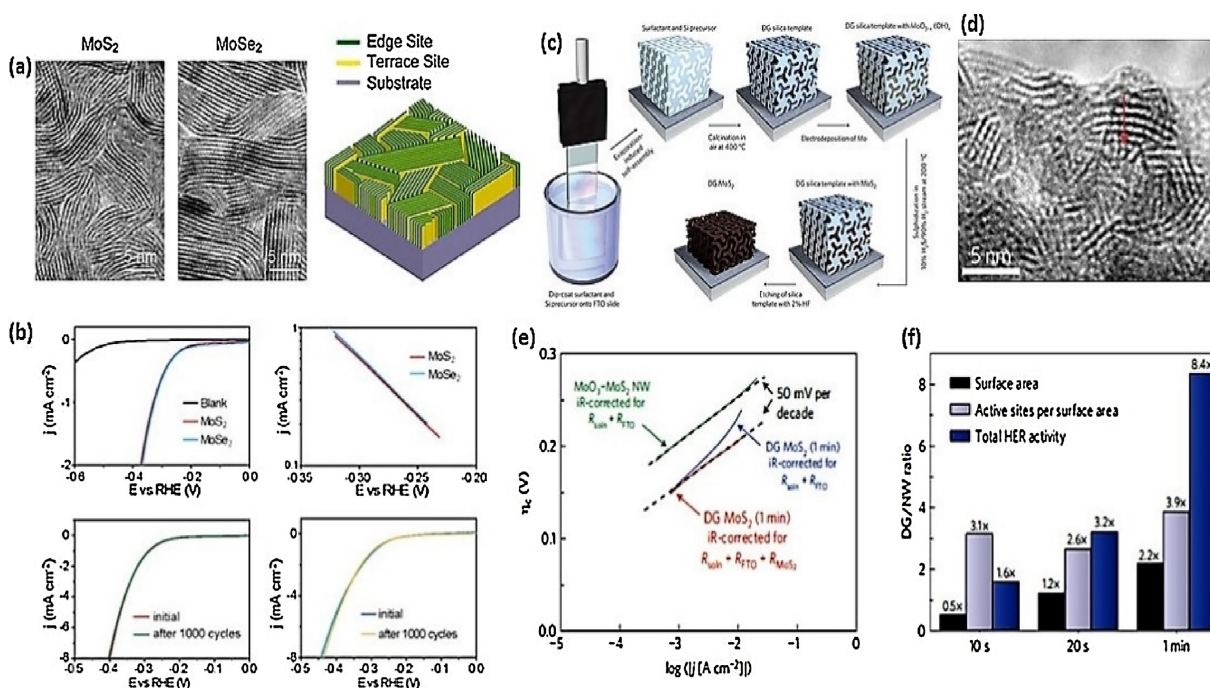

Fig. 34. (a) TEM image of a MoS_2 film fabricated by rapid sulfurization process. (b) Idealized structure of edge-terminated molybdenum chalcogenide films with maximally exposing the edges of the layers. *Reprinted with permission from Kong et al. 37(a) Copyright 2013 American Chemical Society.* (c) Schematic for the synthesis of double-gyroid mesoporous MoS_2 engineered to preferentially expose edge sites for enhanced HER activity. (d) TEM image of thus synthesized MoS_2 film (e) Tafel slope of double-gyroid MoS_2 *v/s* core-shell MoO_3-MoS_2 nanowires, showing the 50 mV per decade slope once corrected for the resistance of the MoS_2. (f) Ratios of surface area, density of active sites per surface area and total HER activity of the various double-gyroid MoS_2 films *v/s* the nanowires. (*Reprinted by permission from Macmillan Publishers Ltd: Nature Materials (Kibsgaard et al. 36(c)), copyright 2012.*)

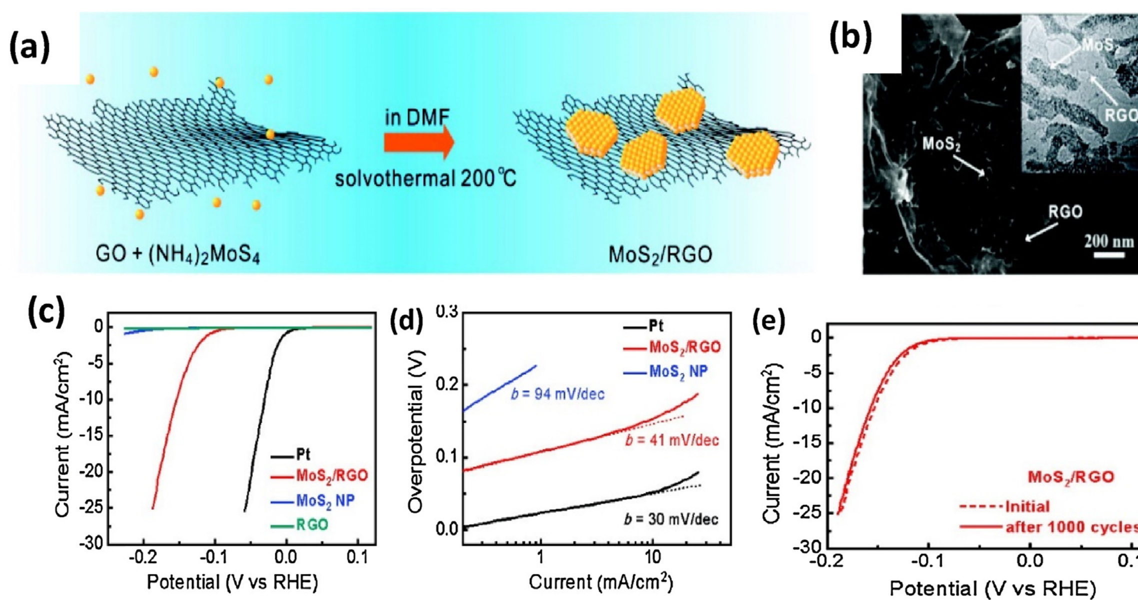

Fig. 35. (a) Scheme for the solvothermal synthesis, (b) SEM and TEM (inset) images of MoS_2-graphene nanocomposite. (c) Polarization curves, (d) Tafel plots recorded on glassy carbon electrodes with a catalyst loading of 0.28 mg/cm^2 and (e) Durability test for the MoS_2/RGO hybrid catalyst. *Reprinted with permission from Li et al. 36(a) Copyright 2011 American Chemical Society.*

including graphene, graphene oxide, carbon nanotubes, and carbon nanofibers, etc. have been most common hosts to fabricate integrated MoS_2 nanostructures [33f-i]. Dai and coworkers reported a selective solvothermal process to synthesize MoS_2 nanoparticles on reduced graphene oxide (RGO) sheets suspended in solution (Fig. 35) [36a]. Thus synthesized, RGO@MoS_2 composite shows excellent electrocatalytic activity at a low catalytic overpotential of ~0.1 V with a smaller Tafel slope of ~41 mV dec^{-1}. The superior performance was observed due to the excellent electrical coupling of the RGO network with MoS_2. Moreover, MoS_2-based hybrid nanocomposites were prepared to utilize graphene foam, carbon nanotubes, and carbon nanofiber as conducting hosts exhibiting excellent catalytic activity [32b,37d]. In a similar experiment, the graphene-deposited 3D-Ni foam was used to fabricate MoSx catalysts for HER applications.

8. Defective MoS_2 nanosheets and amorphous MoS_2

Defect engineering and growth of amorphous molybdenum sulfide (MoS_x) are another efficient way to increase the HER catalytic activity [36d,h]. The defective MoS_2 nanosheets with rich, active sites reported to exhibit improved catalytic activity. On the other hand, amorphous molybdenum sulfide (MoS_x) preserve short-range ordering with the substantial structural disorder; the high surface area and structural defects lead to possessing more catalytic active sites for HER [33e]. The defect-rich MoS_2 exhibited a smaller Tafel slope, lower onset overpotential (~120 mV) and larger cathodic current density as compared to defect-free MoS_2 [36d,38a]. The plasma treatment was suggested as an efficient way to fabricate defect-rich MoS_2 [38b,c] for HER application. The amorphous molybdenum sulfide (MoS_x) was successfully synthesized via electrodeposition or wet chemical reactions demonstrating excellent HER activity [38d,e]. Merki and co-worker reported the effect of transition-metal ions (Mn, Fe, Ni, Co, Cu, and Zn) doping on the HER activity of MoS_x [39a]. It is hard to characterize the atomic structures precisely, categorizing the active catalytic sites, to understand the overall catalytic mechanism(s) for amorphous MoSx catalysts. Even after several attempts, the reaction mechanism of HER activity for amorphous molybdenum sulfide (MoS_x) is not fully understood [38d,39b–e].

9. Role of the phase, edge, and vacancies

Recently, more insights have been provided on the HER catalytic activity using mesoporous (holey) 1T-phase MoS_2 nanosheets (P-1T-MoS_2) synthesized through a liquid ammonia-assisted lithiation route [40a]. The report successfully investigated and compare the contributions of crystal structure (phase), edges, and sulfur vacancies (S vacancies) with mesoporous 2H-phase MoS_2, mesoporous 2H-phase MoS_2 after sulfur compensation, 1T-phase MoS_2, and 2H-phase MoS_2 [40a]. Furthermore, it was revealed that: (1) the 1T phase MoS_2 exhibits superior HER catalytic activity over the 2H phase; (2) an increase in the density of edges, can further improve the catalytic performance; (3) P-1T-MoS_2 deliver better performance as compared to 1T-MoS_2; and (4) the contribution of S vacancies to HER catalysis should not be neglected. As a result from S vacancies and edges, high intrinsic HER activity can be obtained on porous 1T-MoS_2 nanosheets, with a Tafel slope ~43 mV dec^{-1}, which is among the highest performances reported for phase-pure MoS_2. In a recent report by Zhang et al. the HER activities at the edge and basal-plane sites of single-layer MoS_2 synthesized by CVD method were carried out using a local probe method enabled by selected-area lithography. The e-beam lithography was utilized to open reaction windows at sites of interest on poly (methyl methacrylate) (PMMA) covered single layered MoS_2 triangles. The study revealed the improvements in HER activities (i.e., decreased overpotential and lower the Tafel slope) are resultant from the active sites of Mo-terminated edge and 2H to a 1T′ phase transition. Additionally, it was concluded that the active sites on the Mo-terminated edge of both 2H- and 1T′-MoS_2 were critical with optimum HER performance, and the basal-plane activity of 1T′-MoS_2 was favorable for the HER in comparison with 2H counterpart [40a].

10. The photoelectrocatalytic (PEC) HER

Photoelectrochemical (PEC) water splitting is considered as another one of the most auspicious methodologies besides the electrocatalysis to produce hydrogen fuel [31g,8i,32a]. In the PEC HER mechanism, the hydrogen production can be achieved either by a photovoltaics-electrolyzer system or an integrated PEC water-splitting system [31d–f]. The integrated PEC systems for water splitting at the semiconductor interface referred to be more economical promising better efficiency. A typical PEC assembly is composed of two essential components: (1) a light absorber (usually a semiconductor) to produce electron-hole pairs upon light illumination and (2) an electrocatalyst responsible for the charge transfer and to reduce the overpotential for hydrogen production. In a PEC assembly, water splitting could be achieved with either a single semiconductor (bandgap higher than ~1.7 eV) or a combination of two or more semiconductors in a tandem PEC cell [8i]. A typical tandem PEC cell consists of a hydrogen-evolving photocathode and an integrated oxygen-evolving photoanode [31d-f]. A tandem PEC cell comprising more than one semiconducting materials with lower bandgaps enables access to a more substantial part of the solar spectrum as compared to a single semiconductor, thus greatly preferred. The application of TMDCs for photoelectrocatalytic HER has long been investigated [31g,8i,32a]. The semiconducting TMDCs possessing a direct band gap between 1.4–2.3 eV and an indirect band gap of 1.0–1.5 eV will absorb the incident photon with energies equal or above direct/indirect band gap, and show large absorption coefficients (≈106 cm^{-1}) [41]. The heterostructures of TMDCs and metal are reported to effectively enhance the HER activity of a PEC cell assembly due to an increase in the local density of states near the TMDCs/metal interface [41a–d]. Moreover, 1T-MoS_2 exhibit significantly enhanced HER catalytic activity as compared to 2H-MoS_2 [37b]. An integrated PEC cell assembly of planar p-type Si and 1T-MoS_2 (1T-MoS_2@Si) is reported serving as an efficient and robust system for PEC hydrogen production [41b]. Furthermore, it was confirmed that the charge-transfer resistances at the semiconductor/catalyst and catalyst/electrolyte interfaces of 1T-MoS_2/Si is superior to 2H-MoS_2. In another experiment, Lewis and co-worker reported enhanced PEC performance of Pt-decorated p-type WSe_2 photocathodes [42a]. A more detailed and systematic study performed by Chang et al. [42b] examined the relationship between a number of MoS_2 layer and photocatalytic hydrogen generation. As it is well known that the layer number of MoS_2 plays an important role of HER activity. In the experiment designed by Chang et al. [42b], MoS_2 layers varying from 1 to 112 were synthesized loaded with CdS (MoS_2@CdS). The corresponding hydrogen production activities were explored in lactic acid and Na_2S-Na_2SO_3 solutions. From the study, it is observed that the highest H_2 production rate was achieved with MoS_2@CdS has a single-layer assembly confirming that the photocatalytic activity is critically dependent on the number of layer participating (increasing with decreasing MoS_2 layer number) [42b]. Excitingly it was noted that the H2 production rate using MoS2@CdS (single layer assembly) in lactic acid solution (2.59 mmol h^{-1}) is higher than that in the Na_2S-Na_2SO_3 solution (2.01 mmol h^{-1}) which is much higher as compared to Pt/CdS in lactic acid solution (0.44 mmol h^{-1}) [42c]. In a very recent study, a ternary hybrid Cu_2ZnSnS_4 (CZTS)/MoS_2-reduced graphene oxide (RGO) is reported as the promising alternative of noble metals for H_2 generation. The heterostructure exhibit exceptionally higher (~320%) HER activity than bare CZTS as well as Au or Pt decorated CZTS too [42d].

11. Prospects and direction

This brief review is an attempt to highlight the various properties and theoretical aspects of MoS_2 and its use in the field of 2D nanoelectronic devices. Although limited progress has been made in discovering new QSH insulators based on MoS_2 during the recent years, the implementation of robust tools for assessing topological characteristics of band structures (e.g., Z_2

invariant) will help to accelerate the discovery process for various technological applications. The primary challenge in the field of topological materials is to increase the gap to realize high-temperature topological state, which can be met by designing new allotropic forms of MoS_2. Also, the computer mimicking is increasingly used to explore the physics of novel TIs, where new candidates of topological materials are often predicted and designed for experimental synthesis and characterization. DFT-based electronic structure calculations are expected to provide mechanistic insights of the novel TIs based on MoS_2 and future promises for the applications in quantum computing and spintronics. It seems that MoS_2 is just star material for investigation of similar materials to be used in various device applications shortly.

12. Summary

In brief, this review is an attempt to highlight the various properties and theoretical aspects of MoS_2 summering its potential applications in many fields. The excellent electronic, spintronics, sensing and catalytic performance suggested that MoS_2 is a possible substitute for the state of the art materials currently being used in several industries. Even though MoS_2 is an earth-abundant material, reliable and high-quality production, from the fundamental to scalable technological applications is extensively demanded. Challenges including large-scale production, cost, and stability of MoS_2 are critically important. It is obvious to overcome the challenges, reducing the cost will pave the way for mass production while long-term stability guarantees industrial application. Limited progress has been made in discovering new QSH insulators based on MoS_2 during the recent years, the implementation of robust tools for assessing topological characteristics of band structures (e.g., Z_2 invariant) will help to accelerate the discovery process for various technological applications. The primary challenge in the field of topological materials is to increase the gap to realize high-temperature topological state, which can be met by designing new allotropic forms of MoS_2. Also, the computer mimicking is increasingly used to explore the physics of novel TIs, where new candidates of topological materials are often predicted and designed for experimental synthesis and characterization. DFT-based electronic structure calculations are expected to provide mechanistic insights of the novel TIs based on MoS_2 and future promises for the applications in quantum computing and spintronics.

Although MoS_2-based catalysts have shown promising potentials as electrochemical HER catalyst, the development in photoelectrochemical hydrogen production is relatively slower. To the direct realization of solar-to-fuel conversion using MoS_2-based catalysts, the more rigorous efforts are needed. Even after the significant improvement in overall catalytic performance, the HER catalytic activity of MoS_2 is still unable to beat Pt-based noble metals. The in-depth understanding of the catalytic mechanisms on the atomic level is not yet fully defined. It seems that MoS_2 is just a star material, it is strongly suggested that the theoretical and experimental works should be integrated to enable more efficient rational design for various applications.

Acknowledgments

This work was supported by the Department of Science & Technology (DST), Government of India, and partially by National Chemical Laboratory Project MLP-028626. Jai Singh would like to acknowledge UGC-India and DST for providing project under UGC Start-up Grant and DST Fast track.

References

[1] (a) K.S. Novoselov, A. Mishchenko, A. Carvalho, A.H.C. Neto, Science 353 (2016) 9439;
(b) A.K. Geim, K.S. Novoselov, Nat. Mater. 6 (2007) 183–191;
(c) A.K. Geim, Science 324 (2009) 1530–1534;
(d) K.S. Novoselov, A.K. Geim, S.V. Morozov, D. Jiang, Y. Zhang, S.V. Dubonos, I.V. Grigorieva, A.A. Firsov, Science 306 (2004) 666;
(e) D.J. Late, A. Ghosh, K.S. Subrahmanyam, L.S. Panchakarla, S.B. Krupanidhi, C.N.R. Rao, Solid State Commun. 150 (2010) 734–738;
(f) B.H. Nguyen, V.H. Nguyen, Adv. Nat. Sci.: Nanosci. Nanotechnol. 7 (2016) 023002;
(g) G. Jo, M. Choe, S. Lee, W. Park, Y.H. Kahng, T. Lee, Nanotechnology 23 (2012) 112001.

[2] (a) P. Kumar, A.K. Singh, S. Hussain, K.N. Hui, K.S. Hui, J. Eom, J. Jung, J. Singh, Rev. Adv. Sci. Eng. 2 (2013) 238–258;
(b) A.K. Singh, M. Ahmad, V.K. Singh, K. Shin, Y. Seo, J. Eom, ACS Appl. Mater. Interfaces 5 (2013) 5276;
(c) A.K. Singh, M.W. Iqbal, V.K. Singh, M.Z. Iqbal, J.H. Lee, S.H. Chun, K. Shin, J. Eom, Mater. Chem. 22 (2012) 15168;
(d) A.K. Singh, J. Eom, ACS Appl. Mater. Interfaces 6 (2014) 2493–2496;
(e) S. Pang, Y. Hernandez, X. Feng, K. Müllen, Adv. Mater. 23 (2011) 2779–2795;
(f) J. Plutnar, M. Pumera, Z. Sofer, J. Mater. Chem. C (2018), doi:10.1039/C8TC00463C.

[3] (a) T.H. Han, Y. Lee, M. Choi, S.H. Woo, S.H. Bae, B.H. Hong, J.H. Ahn, T.W. Lee, Nat. Photon. 6 (2012) 105–110;
(b) W. Yuan, A. Liu, L. Huang, C. Li, G. Shi, Adv. Mater. 25 (2013) 766–771;
(c) A.D. Smith, F. Niklaus, A. Paussa, S. Vaziri, A.C. Fischer, M. Sterner, F. Forsberg, A. Delin, D. Esseni, P. Palestri, M. Östling, M.C. Lemme, Nano Lett. 13 (2013) 3237–3242;
(d) A.K. Singh, S. Andleeb, J. Singh, H.T. Dung, Y. Seo, J. Eom, Adv. Func. Mater. 24 (2014) 7125–7132;
(e) B. Radisavljevic, M.B. Whitwick, A. Kis, ACS Nano 5 (2011) 9934–9938;
(f) M. Begliarbekov, S. Strauf, C.P. Search, Nanotechnology 22 (2011) 165203;
(g) D. Dutta, A. Hazra, S.K. Hazra, J. Das, S. Bhattacharyya, C.K. Sarkar, S. Basu, Meas. Sci. Technol. 26 (2015) 115104;
(h) S.J. Jeong, H.W. Kim, J. Heo, M.H. Lee, H.J. Song, J. Ku, Y. Lee, Y. Cho, W. Jeon, H. Suh, S. Hwang, S. Park, 2D Mater. 3 (2016) 035027;
(i) J.H. Garcia, Marc Vila, A.W. Cummings, S. Roche, Chem. Soc. Rev. (2018), DOI: 10.1039/C7CS00864C.

[4] (a) O.L. Sanchez, D. Lembke, M. Kayci, A. Radenovic, A. Kis, Nat. Nanotechnol. 8 (2013) 497–501;
(b) W. Zhang, J.K. Huang, C.H. Chen, Y.H. Chang, Y. Cheng, L.J. Li, Adv. Mater. 25 (2013) 3456–3461;
(c) S. Bertolazzi, D. Krasnozhon, A. Kis, ACS Nano. 7 (2013) 3246;
(d) H. Li, Z. Yin, Q. He, H. Li, X. Huang, G. Lu, D.W.H. Fam, A.I.Y. Tok, Q. Zhang, H. Zhang, Small 8 (2012) 63–67;
(e) D.J. Late, Y.K. Huang, B. Liu, J. Acharya, S.N. Shirodkar, J. Luo, A. Yan, D. Charles, U.V. Waghmare, V.P. Dravid, C.N.R. Rao, ACS Nano. 7 (2013) 4879–4891;
(f) P.J. Ko, A. Abderrahmane, N.H. Kim, A. Sandhu, Semicond. Sci. Technol. 32 (2017) 065015.

[5] (a) Y. Hang, B. Zheng, C.F. Zhu, X. Zhang, C.L. Tan, H. Li, B. Chen, J. Yang, J.Z. Chen, Y. Huang, L.H. Wang, H. Zhang, Adv. Mater. 27 (2014) 935–939;
(b) K. Lee, R. Gatensby, N. McEvoy, T. Hallam, G.S. Duesberg, Adv. Mater. 25 (2013) 6699;
(c) M. Acerce, D. Voiry, M. Chhowalla, Nat. Nanotech. 10 (2015) 313–318;
(d) K. Leng, Z.X. Chen, X.X. Zhao, W. Tang, B.B. Tian, C.T. Nai, W. Zhou, ACS Nano 10 (2016) 9208–9215;
(e) L. Cao, S. Yang, W. Gao, Z. Liu, Y. Gong, L. Ma, G. Shi, S. Lei, Y. Zhang, S. Zhang, R. Vajtai, P.M. Ajayan, Small 9 (2013) 2905;
(f) M.W. Lin, L. Liu, Q. Lan, X. Tan, K.S. Dhindsa, P. Zeng, V.M. Naik, M.M.C. Cheng, Z. Zhou, J. Phys. D: Appl. Phys. 45 (2012) 345102.

[6] (a) S. Zhao, T. Hotta, T. Koretsune, K. Watanabe, T. Taniguchi, K. Sugawara, T. Takahashi, H. Shinohara, R. Kitaura, 2D Mater. 3 (2016) 025027;
(b) S. Xu, Z. Wu, H. Lu, Y. Han, G. Long, X. Chen, T. Han, W. Ye, Y. Wu, J. Lin, J. Shen, Y. Cai, Y. He, F. Zhang, R. Lortz, C. Cheng, N. Wang, 2D Mater. 3 (2016) 021007;
(c) T. Paul, S. Ghatak, A. Ghosh, Nanotechnology 27 (2016) 125706;
(d) J. Ahn, P.J. Jeon, S.R.A. Raza, A. Pezeshki, S.W. Min, D.K. Hwang, S. Im, 2D Mater. 3 (2016) 045011;
(e) F. Liu, J. Wang, H. Guo, Nanotechnology 26 (2015) 175201.

[7] (a) D.J. Late, B. Liu, H.S.S.R. Matte, C.N.R. Rao, V.P. Dravid, Adv. Funct. Mater. 22 (2012) 1894–1905;
(b) D.J. Late, B. Liu, J.J. Luo, A.M. Yan, H.S.S.R. Matte, M. Grayson, C.N.R. Rao, V.P. Dravid, Adv. Mater. 24 (2012) 3549–3554;
(c) H.S. Matte, A. Gomathi, A.K. Manna, D.J. Late, R. Datta, S.K. Pati, C.N.R. Rao, Angew. Chem. Int. 49 (2010) 4059–4062;
(d) R.V. Kashid, D.J. Late, S.S. Chou, Y. Huang, M. De, D. Joag, M.A. More, V.P. Dravid, Small 9 (2013) 2730–2734;
(e) S. Bae, H. Kim, Y. Lee, X. Xu, J. Park, Y. Zheng, J. Balakrishnan, T. Lei, R.H. Kim, Y. Song, Y.J. Kim, K.S. Kim, B. Özyilmaz, J.H. Ahn, B.H. Hong, S. Iijima, Nat. Nanotechnol. 5 (2010) 574–578.

[8] (a) D.J. Late, B. Liu, H.S.S.R. Matte, V.P. Dravid, C.N.R. Rao, ACS Nano 6 (2012) 5635–5641;
(b) F. Wang, Z. Wang, Q. Wang, F. Wang, L. Yin, K. Xu, Y. Huang, J. He, Nanotechnology 26 (2015) 292001;
(c) Y.C. Lin, D.O. Dumcencon, Y.S. Huang, K. Suenaga, Nat. Nanotechnol. 9 (2014) 391–396;
(d) R. Kappera, D. Voiry, S.E. Yalcin, B. Branch, G. Gupta, A.D. Mohite, M. Chhowalla, Nat. Mater. 13 (2014) 1128–1134;
(e) N.A.H. Castro, F. Guinea, N.M.R. Peres, K.S. Novoselov, A.K. Geim, Rev. Mod. Phys. 81 (2009) 109–162;
(f) D.S. Schulman, A. Sebastian, D. Buzzell, Y.T. Huang, A.J. Arnold, S. Das, ACS Appl. Mater. & Interfaces 9 (2017) 44617–44624;
(g) Z. He, W. Que, Appl. Mater. Today 3 (2016) 23–56;
(h) E. Benavente, M. Santa Ana, F. Mendizábal, G. González, Coord. Chem. Rev. 224 (2002) 87–109;
(i) Q. Ding, B. Song, P. Xu, S. Jin, Chem 1 (2016) 699–726;
(j) R.J. Toh, Z. Sofer, J. Luxa, D. Sedmidubský, M. Pumera, Chem. Commun. 53 (2017) 3054–3057.
[9] (a) Q.H. Wang, K. Kalantar-Zadeh, A. Kis, J.N. Coleman, M.S. Strano, Nat. Nano. 7 (2012) 699–712;
(b) K.F. Mak, C. Lee, J. Hone, J. Shan, T.F. Heinz, Phys. Rev. Lett. 105 (2010) 136805;
(c) A. Kuc, N. Zibouche, T. Heine, Phys. Rev. B 83 (2011) 245213;
(d) K. Kobayashi, J. Yamauchi, Phys. Rev. B 51 (1995) 17085–17095;
(e) L. Liu, S.B. Kumar, Y. Ouyang, J. Guo, IEEE Trans. Electron Devices 58 (2011) 3042–3047.
[10] (a) Y. Ding, Y. Wang, J. Ni, L. Shi, S. Shi, W. Tang, Physica B 406 (2011) 2254–2260;
(b) S. Lebègue, O. Eriksson, Phys. Rev. B 79 (2009) 115409;
(c) A. Splendiani, L. Sun, Y. Zhang, T. Li, J. Kim, C.Y. Chim, G. Galli, F. Wang, Nano Lett. 10 (2010) 1271–1275;
(d) R.F. Frindt, A.D. Yoffe, Proc. R. Soc. Lond. A 273 (1963) 69–83;
(e) D.C. Elias, R.V. Gorbachev, A.S. Mayorov, S.V. Morozov, A.A. Zhukov, P. Blake, L.A. Ponomarenko, I.V. Grigorieva, K.S. Novoselov, F. Guinea, A.K. Geim, Nat. Phys. 7 (2011) 701–704;
(f) R.F. Frindt, Phys. Rev. 140 (1965) A536–A539;
(g) R.F. Frindt, J. Appl. Phys. 37 (1966) 1928–1929;
(h) F. Wang, Z. Wang, Q. Wang, F. Wang, L. Yin, K. Xu, Y. Huang, J. He, Nanotechnology 26 (2015) 292001;
(i) F. Bonaccorso, A. Lombardo, T. Hasan, Z. Sun, L. Colombo, A.C. Ferrari, Mater. Today 15 (2012) 564–589.
[11] (a) A.S. Mayorov, R.V. Gorbachev, S.V. Morozov, L. Britnell, R. Jalil, L.A. Ponomarenko, P. Blake, K.S. Novoselov, K. Watanabe, T. Taniguchi, A.K. Geim, Nano Lett. 11 (2011) 2396–2399;
(b) K.S. Novoselov, D. Jiang, F. Schedin, T.J. Booth, V.V. Khotkevich, S.V. Morozov, A.K. Geim, Proc. Nat. Acad. Sci. U S A 102 (2005) 10451;
(c) D. Jariwala, V.K. Sangwan, D.J. Late, J.E. Johns, V.P. Dravid, T.J. Marks, L.J. Lauhon, M.C. Hersam, Appl. Phys. Lett. 102 (2013) 173107;
(d) L. Liu, S.B. Kumar, Y. Ouyang, J. Guo, IEEE Trans. Electron Devices 58 (2011) 3042–3047;
(e) R. Fivaz, E. Mooser, Phys. Rev. 163 (1967) 743–755.
[12] (a) K. Lee, et al., Adv. Mater. 23 (2011) 4178–4182;
(b) W. Zhang, J.K. Huang, C.H. Chen, Y.H. Chang, Y.J. Cheng, L.J. Li, Adv. Mater. 25 (2013) 3456–3461;
(c) K. Kaasbjerg, K.S. Thygesen, K.W. Jacobsen, Phys. Rev. B 85 (2012) 115317;
(d) A.C. Ferrari, J.C. Meyer, V. Scardaci, C. Casiraghi, M. Lazzeri, F. Mauri, S. Piscanec, D. Jiang, K.S. Novoselov, S. Roth, A.K. Geim, Phys. Rev. Lett. 97 (2006) 187401–187404;
(e) A. Gupta, G. Chen, P. Joshi, S. Tadigadapa, P.C. Eklund, Nano Lett. 6 (2006) 2667–2673.
[13] (a) D. Graf, F. Molitor, K. Ensslin, C. Stampfer, A. Jungen, C. Hierold, L. Wirtz, Nano Lett. 7 (2007) 238–242;
(b) C. Lee, H. Yan, L.E. Brus, T.F. Heinz, J. Hone, S. Ryu, ACS Nano 4 (2010) 2695–2700;
(c) H. Li, Q. Zhang, C.C.R. Yap, B.K. Tay, T.H.T. Edwin, A. Olivier, D. Baillargeat, Adv. Funct. Mater. 22 (2012) 1385–1390;
(d) B. Chakraborty, H.S.S.R. Matte, A.K. Sood, C.N.R. Rao, J. Raman Spectrosc. 44 (2013) 92–96;
(e) A.G. Bagnall, W.Y. Liang, E.A. Marseglia, B. Welber, Physica B 99 (1980) 343–346.
[14] (a) S. Bertolazzi, J. Brivio, A. Kis, ACS Nano 5 (2011) 9703–9709;
(b) A.C. Gomez, M. Poot, G.A. Steele, H.S.J. Zant, N. Agraït, G.R. Bollinger, Adv. Mater. 24 (2012) 772–775;
(c) B. Radisavljevic, A. Radenovic, J. Brivio, V. Giacometti, A. Kis, Nat. Nanotechnol. 6 (2011) 147–150;
(d) W. Zhao, Z. Ghorannevis, L. Chu, M. Toh, K. Kloc, P.H. Tan, G. Eda, ACS Nano 7 (2013) 791–797.
[15] (a) R.M. Martin, Electronic structure Basic Theory and Practical Methods, Cambridge University Press, 2004;
(b) J.G. Lee, Computational Materials Science: An introduction, CRC Press, New York, 2012;
(c) G. Kresse, J. Furthmuller, Phys. Rev. B 54 (1996) 11169;
(d) A. Bansil, H. Lin, T. Das, Reviews of Modern Physics 88 (2016) 021004.
[16] (a) W. Kohn, Rev. Mod. Phys. 71 (1999) 1253;
(b) R. Prasad, Electronic Structure of Materials, CRC Press, New York, 2014.
[17] (a) K.F. Mak, C. Lee, J. Hone, J. Shan, T.F. Heinz, Phys. Rev. Lett. 105 (2010) 136805;
(b) A. Kuc, N. Zibouche, T. Heine, Phys. Rev. B 83 (2011) 245213;
(c) A. Kumar, P.K. Ahluwalia, Eur. Phys. J. B 85 (2012) 186;
(d) A. Kumar, P.K. Ahluwalia, Mater. Chem. Phys. 135 (2012) 755;
(e) A. Splendiani, L. Sun, Y. Zhang, T. Li, J. Kim, C.Y. Chim, G. Galli, F. Wang, Nano Lett. 10 (2010) 1271;
(f) G.R. Bhimanapati, Z. Lin, V. Meunier, Y. Jung, J. Cha, S. Das, D. Xiao, Y. Son, M.S. Strano, X. Valentino, R. Cooper, O.L. Liang, S.G. Louie, E. Ringe, W. Zhou, S.S. Kim, R.R. Naik, B.G. Sumpter, H. Terrones, F. Xia, Y. Wang, J. Zhu, D. Akinwande, N. Alem, J.A. Schuller, R.E. Schaak, M. Terrones, J.A. Robinson, ACS Nano 9 (2015) 11509.
[18] (a) J.B. Sun, J.B. Hannon, R.M. Tromp, P. Johari, A.A. Bol, V.B. Shenoy, K. Pohl, ACS Nano 4 (2010) 7073;
(b) W.Y. Liang, S.L. Cundi, Phis. Mag. 19 (1969) 1031;
(c) J.M. Soler, E. Artacho, J.D. Gale, A. Garcia, J. Junquera, P. Ordejon, D. Sanchez-Portal, J. Phys.: Condens. Matter 14 (2002) 2745;
(d) A. Kumar, P.K. Ahluwalia, Physica B 407 (2012) 4627;
(e) P. Johari, V.B. Shenoy, ACS Nano 5 (2011) 5903;
(f) J.N. Coleman, M. Lotya, A. O'Neill, S.D. Bergin, P.J. King, U. Khan, K. Young, A. Gaucher, S. De, R.J. Smith, I.V. Shvets, S.K. Arora, G. Stanton, H.Y. Kim, K. Lee, G.T. Kim, G.S. Duesberg, T. Hallam, J.J. Boland, J.J. Wang, J.F. Donegan, J.C. Grunlan, G. Moriarty, A. Shmeliov, R.J. Nicholls, J.M. Perkins, E.M. Grieveson, K. Theuwissen, D.W. McComb, P.D. Nellist, V. Nicolosi, Science 331 (2011) 568;
(g) D. Penn, Phys. Rev. B 128 (1962) 2093.
[19] (a) K. Klitzing, G. Dorda, M. Pepper, Phys. Rev. Lett. 45 (1980) 494;
(b) D.J. Thouless, M. Kohmoto, M.P. Nightingale, M. den-Nijs, Phys. Rev. Lett. 49 (1982) 405–408;
(c) F.D.M. Haldane, Phys. Rev. Lett. 61 (1988) 2015–2018;
(d) C.L. Kane, E.J. Mele, Phys. Rev. Lett. 95 (2005) 226801;
(e) C.L. Kane, E.J. Mele, Phys. Rev. Lett. 95 (2005) 146802;
(f) L. Fu, C.L. Kane, E.J. Mele, Phys. Rev. Lett. 98 (2007) 106803;
(g) M.Z. Hasan, C.L. Kane, Rev. Modern Phys. 82 (2010) 3045–3067.
[20] (a) B.A. Bernevig, T.A. Hughes, S.C. Zhang, Science 314 (2006) 1757–1761;
(b) D. Hsieh, D. Qian, L. Wray, Y. Xia, Y.S. Hor, R.J. Cava, M.Z. Hasan, Nature 452 (2008) 970;
(c) L. Fu, C.L. Kane, Phys. Rev. B 76 (2007) 045302;
(d) L. Kou, Y. Ma, Z. Sun, T. Heine, T. Chen, J. Phys. Chem. Lett. 8 (2017) 1905–1919.
[21] (a) G. Eda, T. Fujita, H. Yamaguchi, D. Voiry, M. Chen, M. Chhowalla, ACS Nano 6 (2012) 7311;
(b) X. Qian, J. Liu, L. Fu, J. Li, Science 346 (2014) 1344–1347;
(c) J. Wunderlich, B. Park, A.C. Irvine, L.P. Zarbo, E. Rozkotova, P. Nemec, V. Novak, J. Sinova, T. Jungwirth, Science 330 (2010) 1801;
(d) D. Pesin, A.H. MacDonald, Nat. Mater. 11 (2012) 409;
(e) C.H. Li, O.M.J. van't Erve, J.T. Robinson, Y. Liu, L. Li, B.T. Jonker, Nat. Nanotechnol. 9 (2014) 218–224;
(f) L. Liu, J. Guo, J. Appl. Phys. 118 (2015) 124502;
(g) H. Yang, S.W. Kim, M. Chhowalla, Y.H. Lee, Nat. Phys. 13 (2017) 931.
[22] (a) Y. Sun, C. Felser, B. Yan, Phys. Rev. B 92 (2015) 165421;
(b) S.M. Nie, Z. Song, H. Weng, Z. Fang, Phys. Rev. B 91 (2015) 235434;
(c) Y. Ma, L. Kou, X. Li, Y. Dai, S.C. Smith, T. Heine, Phys. Rev. B 92 (2015) 085427;
(d) Y. Ma, L. Kou, X. Li, Y. Dai, T. Heine, Phys. Rev. B 93 (2016) 035442;
(e) A.M. van der Zande, P.Y. Huang, D.A. Chenet, T.C. Berkelbach, Y. You, G.H. Lee, T.F. Heinz, D.R. Reichman, D.A. Muller, J.C. Hone, Nat. Mater. 12 (2013) 554.
[23] (a) Y.L. Chen, J.G. Analytis, J.H. Chu, Z.K. Liu, S.K. Mo, X.L. Qi, H.J. Zhang, D.H. Lu, X. Dai, Z. Fang, S.C. Zhang, I.R. Fisher, Z. Hussain, Z.X. Shen, Science 325 (2009) 178;
(b) Y. Xu, B.H. Yan, H.J. Zhang, J. Wang, G. Xu, P. Tang, W.H. Duan, S.C. Zhang, Phys. Rev. Lett. 111 (2013) 136804;
(c) Y.D. Ma, Y. Dai, L.Z. Kou, T. Frauenheim, T. Heine, Nano Lett. 15 (2015) 1083;
(d) P.F. Liu, L. Zhou, T. Frauenheim, L.M. Wu, Nanoscale 9 (2016) 4915.
[24] (a) M.Y. Li, Y. Shi, C.C. Cheng, L.S. Lu, Y.C. Lin, H.L. Tang, M.L. Tsai, C.W. Chu, K.H. Wei, J.H. He, W.H. Chang, K. Suenaga, L.J. Li, Science 349 (2015) 524;
(b) M.H. Chiu, C. Zhang, H.W. Shiu, C.P. Chuu, C.H. Chen, C.Y. Chang, C.H. Chen, M.Y. Chou, C.K. Shih, L.J. Li, Nat. Commun. 6 (2015) 7666;
(c) M.H. Chiu, M.Y. Li, W. Zhang, W.T. Hsu, W.H. Chang, M. Terrones, H. Terrones, L.J. Li, ACS Nano 8 (2014) 9649;
(d) T.H. Ly, M.H. Chiu, M.Y. Li, J. Zhao, D.J. Perello, M.O. Cichocka, H.M. Oh, S.H. Chae, H.Y. Jeong, F. Yao, L.J. Li, Y.H. Lee, ACS Nano 8 (2014) 11401–11408;
(e) J.K. Huang, J. Pu, C.L. Hsu, M.H. Chiu, Z.Y. Juang, Y.H. Chang, W.H. Chang, Y. Iwasa, T. Takenobu, L.J. Li, ACS Nano 8 (2014) 923.
[25] (a) C.H. Chen, C.L. Wu, J. Pu, M.H. Chiu, P. Kumar, T. Takenobu, L.J. Li, 2D Mater 1 (2014) 034001;
(b) Y.C. Lin, W. Zhang, J.K. Huang, K.K. Li, Y.H. Lee, C.T. Liang, C.W. Chu, L.J. Li, Nanoscale 4 (2012) 6637–6641;
(c) Y.H. Lee, X.Q. Zhang, W. Zhang, M.T. Chang, C.T. Lin, K.D. Chang, Y.C. Yu, J.T.W. Wang, C.S. Chang, L.J. Li, T.W. Lin, Adv. Mater. 24 (2012) 2320–2325;
(d) G.H. Han, et al., Nano Lett. 11 (2011) 4144–4148;
(e) J. Gao, J. Yip, J. Zhao, B.I. Yakobson, F. Ding, J. Am. Chem. Soc. 133 (2011) 5009–5015.
[26] (a) Y. Zhan, Z. Liu, S. Najmaei, P.M. Ajayan, J. Lou, Small 8 (2012) 966–971;
(b) K.K. Liu, et al., Nano Lett. 12 (2012) 1538–1544;

(c) Z. Guo, H. Zhang, S. Lu, Z. Wang, S. Tang, J. Shao, Z. Sun, H. Xie, H. Wang, X.-F. Yu, P.K. Chu, Adv. Funct. Mater. 25 (2015) 6996–7002;
(d) P. Joensen, R.F. Frindt, S.R. Morrison, Mater. Res. Bull. 21 (1986) 457–461;
(e) W.M.R. Divigalpitiya, S.R. Morrison, R.F. Frindt, Thin Solid Films 186 (1990) 177–192;
(f) A.H. Woomer, T.W. Farnsworth, J. Hu, R.A. Wells, C.L. Donley, S.C. Warren, ACS Nano 9 (2015) 8869–8884.

[27] (a) W.M.R. Divigalpitiya, R.F. Frindt, S.R. Morrison, Science 246 (1989) 369–371;
(b) S. Kirmayer, E. Aharon, E. Dovgolevsky, M. Kalina, G.L. Frey, Philos. Trans. R. Soc. A 365 (2007) 1489–1508;
(c) G.L. Frey, K.J. Reynolds, R.H. Friend, H. Cohen, Y. Feldman, J. Am. Chem. Soc. 125 (2003) 5998–6007;
(d) J. Heising, M.G. Kanatzidis, J. Am. Chem. Soc. 121 (1999) 638–643;
(e) M.A. Py, R.R. Haering, Can. J. Phys. 61 (1983) 76–84;
(f) M.A. Bissett, I.A. Kinloch, R.A.W. Dryfe, ACS Appl. Mater. Interfaces 7 (2015) 17388–17398;
(g) S. Wu, Z. Zeng, Q. He, Z. Wang, S.J. Wang, Y. Du, Z. Yin, X. Sun, W. Chen, H. Zhang, Small 8 (2012) 2264–2270.

[28] (a) G. Eda, H. Yamaguchi, D. Voiry, T. Fujita, M.W. Chen, M. Chhowalla, Nano Lett. 11 (2011) 5111–5116;
(b) S. Hussain, J. Singh, D. Vikraman, A.K. Singh, M.Z. Iqbal, M.F. Khan, P. Kumar, D.C. Choi, W. Song, K.S. An, J. Eom, W.G. Lee, J.W. Jung, Scientific Reports 6 (2016) 30791;
(c) S. Hussain, M.A. Shehzad, D. Vikraman, M.F. Khan, J. Singh, D.C. Choi, Y. Seo, J. Eom, W.G. Lee, J.W. Jung, Nanoscale 8 (2016) 4340–4347;
(d) L.K. Tan, B. Liu, J.H. Teng, S. Guo, H.Y. Lowd, K.P. Loh, Nanoscale 6 (2014) 10584–10588;
(e) B.D. Keller, A. Bertuch, J. Provine, G. Sundaram, N. Ferralis, J.C. Grossman, Chem. Mater. 29 (2017) 2024–2032.

[29] (a) V. Podzorov, M.E. Gershenson, C. Kloc, R. Zeis, E. Bucher, Appl. Phys. Lett. 84 (2004) 3301–3303;
(b) S. Walia, S. Balendhran, Y. Wang, A. Kadir, R. Zoolfakar, A. Atkin, P. Ou, J. Sriram, S. Kalantar, K. Zadeh, M. Bhaskaran, Appl. Phys. Lett. 103 (2013) 232105;
(c) J.H. Kang, W. Liu, K. Banerjee, Appl. Phys. Lett. 104 (2014) 093106;
(d) J. Yoon, W. Park, G.Y. Bae, Y. Kim, H.S. Jang, Y. Hyun, S.K. Lim, Y.H. Kahng, W.K. Hong, B.H. Lee, Small (2019) 3295–3300;
(e) Y.T. Lee, K. Choi, H.S. Lee, S.W. Min, P.J. Jeon, D.K. Hwang, H.J. Choi, S. Im, Small 10 (2014) 2356–2361;
(f) S. Andleeb, J. Eom, N.R. Naz, A.K. Singh, J. Mater. Chem. C 5 (2017) 8308.

[30] (a) S. Das, R. Gulotty, A.V. Sumant, A. Roelofs, Nano Lett. 14 (2014) 2861–2866;
(b) T. Roy, M. Tosun, J.S. Kang, A.B. Sachid, S.B. Desai, M. Hettick, C.C. Hu, A. Javey, ACS Nano 8 (2014) 6259–6264;
(c) A.K. Singh, C. Hwang, J. Eom, ACS Appl. Mater. Interfaces 8 (2016) 34699–34705;
(d) A.K. Singh, S. Andleeb, J. Singh, J. Eom, RSC Adv. 5 (2015) 77014–77018;
(e) A.K. Singh, R.K. Pandey, R. Prakash, J. Eom, Appl. Surf. Sci. 437 (2018) 70–74;
(f) M. Shanmugam, C.A. Durcan, B. Yu, Nanoscale 4 (2012) 7399–7405.

[31] (a) S. Chu, A. Majumdar, Nature 488 (2012) 294–303;
(b) J.A. Turner, Science 305 (2004) 972–974;
(c) N.S. Lewis, D.G. Nocera, Proc. Natl. Acad. Sci. USA 103 (2006) 15729–15735;
(d) M.G. Walter, E.L. Warren, J.R. McKone, S.W. Boettcher, Q.X. Mi, E.A. Santori, N.S. Lewis, Chem. Rev. 110 (2010) 6446–6473;
(e) A.J. Bard, M.A. Fox, Acc. Chem. Res. 28 (1995) 141–145;
(f) J.R. McKone, N.S. Lewis, H.B. Gray, Chem. Mater. 26 (2014) 407–414;
(g) A. Fujishima, K. Honda, Nature 238 (1972) 37–38.

[32] (a) J.O.M. Bockris, E.C. Potter, J. Electrochem. Soc. 99 (1952) 169–186;
(b) Y. Yan, X. Ge, Z. Liu, J.Y. Wang, J.M. Lee, X. Wang, Nanoscale 5 (2013) 7768–7771;
(c) X. Guo, G.I. Cao, F. Ding, X. Li, S. Zhen, Y. Xue, Y. Yan, T. Liu, K.J. Sun, Mater. Chem. A 3 (2015) 5041–5046;
(d) A.B. Laursen, A.S. Varela, F. Dionigi, H. Fanchiu, C. Miller, O.L. Trinhammer, J. Rossmeisl, S.J. Dahl, Chem. Educ. 89 (2012) 1595–1599;
(e) J.K. Norskov, T. Bligaard, A. Logadottir, J.R. Kitchin, J.G. Chen, S. Pandelov, J.K. Norskov, J. Electrochem. Soc. 152 (2005) J23–J26;
(f) B. Hinnemann, P.G. Moses, J. Bonde, K.P. Jorgensen, J.H. Nielsen, S. Horch, I. Chorkendorff, J.K. Norskov, J. Am. Chem. Soc. 127 (2005) 5308–5309;
(g) J. Greeley, T.F. Jaramillo, J. Bonde, I.B. Chorkendorff, J.K. Norskov, Nat. Mater. 5 (2006) 909–913.

[33] (a) M.S. Faber, S. Jin, Energy Environ. Sci. 7 (2014) 3519–3542;
(b) M. Zeng, Y.G. Li, J. Mater. Chem. A 3 (2015) 14942–14962;
(c) J.D. Benck, T.R. Hellstern, J. Kibsgaard, P. Chakthranont, T.F. Jaramillo, ACS Catal. 4 (2014) 3957–3971;
(d) A.B. Laursen, S. Kegnaes, S. Dahl, I. Chorkendorff, Energy Environ. Sci. 5 (2012) 5577–5591;
(e) C.G. Morales-Guio, X.L. Hu, Acc. Chem. Res. 47 (2014) 2671–2681;
(f) S. Jayabal, G. Saranya, J. Wu, Y. Liu, D. Geng, X. Meng, J. Mater. Chem. A 5 (2017) 24540–24563;
(g) A. Eftekhari, Appl. Mater. Today 8 (2017) 1–17;
(h) M. Velický, P.S. Toth, Appl. Mater. Today 8 (2017) 68–103;
(i) L. Yang, P. Liu, J. Li, B. Xiang, Catalysts 7 (2017) 285, http://dx.doi.org/10.3390/catal7100285.

[34] (a) M.S. Faber, R. Dziedzic, M.A. Lukowski, N.S. Kaiser, Q. Ding, S. Jin, J. Am. Chem. Soc. 136 (2014) 10053–10061;
(b) M. Caban-Acevedo, M.L. Stone, J.R. Schmidt, J.G. Thomas, Q. Ding, H.C. Chang, M.L. Tsai, J.H. He, S. Jin, Nat. Mater. 14 (2015) 1245–1251;
(c) P.C.K. Vesborg, B. Seger, I. Chorkendorff, J. Phys. Chem. Lett. 6 (2015) 951–957;
(d) E.J. Popczun, J.R. McKone, C.G. Read, A.J. Biacchi, A.M. Wiltrout, N.S. Lewis, R.E. Schaak, J. Am. Chem. Soc. 135 (2013) 9267–9270;
(f) J.F. Callejas, C.G. Read, C.W. Roske, N.S. Lewis, R.E. Schaak, Chem. Mater. 28 (2016) 6027–6044.

[35] (a) M. Chhowalla, H.S. Shin, G. Eda, L.J. Li, K.P. Loh, H. Zhang, Nat. Chem. 5 (2013) 263–275;
(b) M.S. Xu, T. Liang, M.M. Shi, H.Z. Chen, Chem. Rev. 113 (2013) 3766–3798;
(c) Q.H. Wang, K. Kalantar-Zadeh, A. Kis, J.N. Coleman, M.S. Strano, Nat. Nano 7 (2012) 699–712;
(d) D. Merki, X.L. Hu, Energy Environ. Sci. 4 (2011) 3878–3888;
(e) H.I. Karunadasa, E. Montalvo, Y. Sun, M. Majda, J.R. Long, C.J. Chang, Science 335 (2012) 698–702;
(f) H. Tributsch, J.C. Bennett, J. Electroanal. Chem. 81 (1977) 97–111.

[36] (a) Y.G. Li, H.L. Wang, L.M. Xie, Y.Y. Liang, G.S. Hong, H.J. Dai, J. Am. Chem. Soc. 133 (2011) 7296–7299;
(b) T.F. Jaramillo, K.P. Jørgensen, J. Bonde, J.H. Nielsen, S. Horch, I. Chorkendorff, Science 317 (2007) 100–102;
(c) J. Kibsgaard, Z.B. Chen, B.N. Reinecke, T.F. Jaramillo, Nat. Mater. 11 (2012) 963–969;
(d) J. Xie, H. Zhang, S. Li, R. Wang, X. Sun, M. Zhou, J. Zhou, X.W. Lou (David), Y. Xie, Adv. Mater. 25 (2013) 5807–5813;
(e) D.Y. Chung, S.K. Park, Y.H. Chung, S.H. Yu, D.H. Lim, N. Jung, H.C. Ham, H.Y. Park, Y. Piao, S.J. Yoo, Y.E. Sung, Nanoscale 6 (2014) 2131;
(f) G. Ye, Y. Gong, J. Lin, B. Li, Y. He, S.T. Pantelides, W. Zhou, R. Vajtai, P.M. Ajayan, Nano Lett. 16 (2016) 1097;
(g) H. Li, C. Tsai, A.L. Koh, L. Cai, A.W. Contryman, A.H. Fragapane, J. Zhao, H.S. Han, H.C. Manoharan, F. Abild-Pedersen, Nat. Mater. 15 (2016) 48;
(h) J. Luxa, V. Mazánek, D. Bouša, D. Sedmidubský, M. Pumera, Z. Sofer, ChemElectroChem 3 (2016) 565–571.

[37] (a) D.S. Kong, H.T. Wang, J.J. Cha, M. Pasta, K.J. Koski, J. Yao, Y. Cui, Nano Lett 13 (2013) 1341–1347;
(b) M.A. Lukowski, A.S. Daniel, F. Meng, A. Forticaux, L.S. Li, S. Jin, J. Am. Chem. Soc. 135 (2013) 10274–10277;
(c) L. Yang, H. Hong, Q. Fu, Y.F. Huang, J.Y. Zhang, X.D. Cui, Z.Y. Fan, K.H. Liu, B. Xiang, ACS Nano 9 (2015) 6478–6483;
(d) L. Liao, J. Zhu, X.J. Bian, L.N. Zhu, M.D. Scanlon, H.H. Girault, B.H. Liu, Adv. Funct. Mater. 23 (2013) 5326–5333.

[38] (a) J. Xie, J. Zhang, S. Li, F. Grote, X. Zhang, H. Zhang, R. Wang, Y. Lei, B. Pan, Y. Xie, J. Am. Chem. Soc. 135 (2013) 17881–17888;
(b) L. Tao, X. Duan, C. Wang, X. Duan, S. Wang, Chem. Commun. 51 (2015) 7470–7473;
(c) G. Ye, Y. Gong, J. Lin, B. Li, Y. He, S.T. Pantelides, W. Zhou, R. Vajtai, P.M. Ajayan, Nano Lett 16 (2016) 1097–1103;
(d) D. Merki, S. Fierro, H. Vrubel, X.L. Hu, Chem. Sci. 2 (2011) 1262–1267;
(e) H. Vrubel, X.L. Hu, ACS Catal. 3 (2013) 2002–2011.

[39] (a) D. Merki, H. Vrubel, L. Rovelli, S. Fierro, X.L. Hu, Chem. Sci. 3 (2012) 2515–2525;
(b) J.D. Benck, Z.B. Chen, L.Y. Kuritzky, A.J. Forman, T.F. Jaramillo, ACS Catal. 2 (2012) 1916–1923;
(c) H. Vrubel, D. Merki, X.L. Hu, Energy Environ. Sci. 5 (2012) 6136–6144;
(d) Y.F. Huang, R.J. Nielsen, W.A. Goddard, M.P. Soriaga, J. Am. Chem. Soc. 137 (2015) 6692–6698;
(e) P.D. Tran, T.V. Tran, M. Orio, S. Torelli, Q.D. Truong, K. Nayuki, Y. Sasaki, S.Y. Chiam, R. Yi, I. Honma, et al., Nat. Mater. 15 (2016) 640.

[40] (a) Y. Yin, J. Han, Y. Zhang, X. Zhang, P. Xu, Q. Yuan, L. Samad, X. Wang, Y. Wang, Z. Zhang, et al., J. Am. Chem. Soc. 13 (2016) 7965–7972;
(b) J. Zhang, J. Wu, H. Guo, W. Chen, J. Yuan, U. Martinez, G. Gupta, A.D. Mohite, P.M. Ajayan, J. Lou, Adv. Mater. 29 (2017) 1701955.

[41] (a) J.M. Velazquez, J. John, D.V. Esposito, A. Pieterick, R. Pala, G. Sun, X. Zhou, Z. Huang, S. Ardo, M.P. Soriaga, et al., Energy Environ. Sci. 9 (2016) 164–175;
(b) Y. Qi, Q. Xu, Y. Wang, B. Yan, Y. Ren, Z. Chen, ACS Nano 10 (2016) 2903–2909;
(c) M. Velický, M.A. Bissett, C.R. Woods, P.S. Toth, T. Georgiou, I.A. Kinloch, K.S. Novoselov, R.A.W. Dryfe, Nano Lett. 16 (2016) 2023–2032;
(d) J. Wong, D. Jariwala, G. Tagliabue, K. Tat, A.R. Davoyan, M.C. Sherrott, H.A. Atwater, ACS Nano. 11 (2017) 7230–7240;
(e) D. Jariwala, A.R. Davoyan, G. Tagliabue, M.C. Sherrott, J. Wong, H.A. Atwater, Nano Lett. 16 (2016) 5482–5487.

[42] (a) Q. Ding, F. Meng, C.R. English, M. Caban-Acevedo, M.J. Shearer, D. Liang, A.S. Daniel, R.J. Hamers, S. Jin, J. Am. Chem. Soc. 136 (2014) 8504–8507;
(b) K. Chang, M. Li, T. Wang, S. Ouyang, P. Li, L. Liu, J. Ye, Adv. Energy Mater. 5 (2015);
(c) K. Chang, Z. Mei, T. Wang, Q. Kang, S. Ouyang, J. Ye, ACS Nano. 8 (2014) 7078–7087;
(d) E. Ha, W. Liu, L. Wang, H.W. Man, L. Hu, S.C.E. Tsang, C.T.L. Chan, W.M. Kwok, L.Y.S. Lee, K.Y. Wong, Sci. Reports 7 (2017) 39411.